

# Transmittance assisted interpretation of nerve fiber orientations

Miriam Menzel<sup>1,2,\*</sup>, Markus Axer<sup>1</sup>, Hans De Raedt<sup>3</sup>, Irene Costantini<sup>4</sup>, Ludovico Silvestri<sup>4</sup>, Francesco Saverio Pavone<sup>4,5</sup>, Katrin Amunts<sup>1,6</sup> & Kristel Michielsen<sup>7</sup>

The neuroimaging technique Three-dimensional Polarized Light Imaging (3D-PLI) is used to reconstruct the brain's nerve fiber architecture by transmitting polarized light through histological brain sections and measuring their birefringence. Here, we demonstrate in experimental studies that the polarization-independent transmitted light intensity (transmittance) significantly decreases with increasing out-of-plane angle of the fibers (by more than 50%). Using finite-difference time-domain simulations, we emulate the experiment and show that this decrease is mainly caused by polarization-independent light scattering in combination with the finite numerical aperture of the imaging system, and that the transmittance does not depend on the crossing angle between in-plane fibers. By combining simulation results and experimental data, we demonstrate that the transmittance can be used to distinguish between in-plane crossing fibers and out-of-plane fibers, which is not possible in standard 3D-PLI measurements. As the transmittance does not depend on the polarization of light, our results are also relevant for other microscopy techniques.

**Keywords:** *polarization microscopy; attenuation; scattering; nerve fiber architecture; brain structure; fibrous structures*

---

<sup>1</sup>Institute of Neuroscience and Medicine (INM-1), Forschungszentrum Jülich GmbH, 52425 Jülich, Germany. <sup>2</sup>Department of Physics, RWTH Aachen University, 52056 Aachen, Germany. <sup>3</sup>Zernike Institute for Advanced Materials, University of Groningen, 9747AG Groningen, the Netherlands. <sup>4</sup>European Laboratory for Non-Linear Spectroscopy, University of Florence, 50019 Sesto Fiorentino, Italy. <sup>5</sup>Department of Physics, University of Florence, 50019 Sesto Fiorentino, Italy. <sup>6</sup>Cécile and Oskar Vogt Institute of Brain Research, University of Düsseldorf, 40204 Düsseldorf, Germany. <sup>7</sup>Jülich Supercomputing Centre, Forschungszentrum Jülich GmbH, 52425 Jülich, Germany.

\* Correspondence and requests for material should be addressed to M.M. (email: [m.menzel@fz-juelich.de](mailto:m.menzel@fz-juelich.de))

UNRAVELING the brain’s nerve fiber architecture is considered to be a key challenge for understanding the brain’s structure and function. One possibility to access the nerve fiber architecture at microscopic resolution is to slice the brain into histological sections and study the light transmitted through these sections. Common transmission microscopy techniques only obtain information about the 2D (in-plane) orientation of the nerve fibers. To reveal the fiber orientations in 3D, other imaging techniques are required.

*Three-dimensional Polarized Light Imaging (3D-PLI)* introduced by AXER et al. [1, 2] reveals the three-dimensional nerve fiber architecture of whole post-mortem brain sections with micrometer resolution. The fiber orientations are obtained by transmitting polarized light through unstained histological brain sections and measuring their birefringence (axes of optical anisotropy) with a polarimeter. The birefringence is caused e. g. by regular fiber arrangements and by the highly anisotropic structure of the myelin sheaths [3] which surround most of the axons in the white matter. In the following, we restrictively use the term *nerve fiber* for myelinated axons.

Especially challenging is the reconstruction of the out-of-plane orientation (*inclination*) angle  $\alpha$  of the nerve fibers. Regions with vertical fibers ( $\alpha = 90^\circ$ ), regions with horizontal  $90^\circ$ -crossing fibers ( $\alpha = 0^\circ$ ), and regions with a low fiber density cannot be distinguished by 3D-PLI because they all yield small birefringence signals [4].

In this paper, we demonstrate that the polarization-independent transmitted light intensity (*transmittance*) can be used to distinguish between these regions because the transmittance strongly depends on the fiber inclination angle, but not on the in-plane crossing angle of the fibers. We show that our findings also hold for microscopy techniques that use unpolarized light.

The transmittance is a measure of how much the light is attenuated when it passes through the brain tissue, i. e. it depends on tissue absorption as well as scattering of light. In previous studies [5], we have shown that polarization-dependent attenuation (*diattenuation*) of brain tissue is mostly less than 5% and cannot explain the observed inclination dependence of the transmittance. As the absorption coefficients of brain matter are small (less than  $0.1 \text{ mm}^{-1}$  [6, 7]), the observed transmittance effects are probably mainly caused by scattering.

To learn more about the observed transmittance effects, we employed *finite-difference time-domain (FDTD)* simulations which enable to study complex light-matter-interactions like scattering: the propagation of the polarized light wave through the brain tissue is modeled by approximating Maxwell’s equations by finite differences and computing the components of the electromagnetic field in space and time. Following a bottom-up approach, we identified the simplest possible model that best describes the experimental observations.

The paper is organized as follows: First, we present various experimental studies which demonstrate that the transmittance decreases significantly with increasing inclination angle of the nerve fibers (by more than 50%). Subsequently, the results of the FDTD simulations are described in which we studied simulated transmittance images for artificial nerve fiber bundles with different inclination angles and different in-plane crossing angles. The simulations show that the decrease in transmittance is mainly caused by isotropic light scattering and by the finite

numerical aperture of the imaging system, and that the transmittance is independent of the in-plane crossing angle of the fibers. Finally, we combine the simulation results with experimental data to demonstrate that the transmittance can indeed be used to distinguish between in-plane crossing and out-of-plane fiber structures.

## RESULTS

**Transmittance of inclined nerve fiber structures.** To investigate the inclination dependence of the transmittance independently from tissue composition and preparation, we performed different studies on  $60 \mu\text{m}$  thin brain sections from various species and subjects. The *normalized transmittance*  $I_{T,N}$  of the brain sections was obtained from 3D-PLI measurements with an effective object-space resolution of  $1.33 \mu\text{m}/\text{px}$  (see [Methods](#)). The strength of the measured birefringence signal (*retardation*  $|\sin \delta|$ ) served as a measure of the fiber inclination angle  $\alpha$  because  $\delta$  decreases with increasing inclination ( $\delta \propto \cos^2 \alpha$  [3]). Additional information about the fiber inclination was gained from brain atlases and *two-photon fluorescence microscopy (TPFM)* measurements.

First, the transmittance was examined in coronal and sagittal sections of rat and vervet monkey brains (see Fig. 1). As the sagittal plane is oriented perpendicularly to the coronal plane, the transmittance of a certain brain region can be evaluated for *flat* fibers ( $\alpha < 45^\circ$ ) in one section plane and for *steep* fibers ( $\alpha > 45^\circ$ ) in the other section plane. The coronal (sagittal) section planes are indicated by blue (red) lines in the respective other brain section for reference. Selected white and gray matter structures are labeled according to rat [8–10] and vervet [11–13] brain atlases. The transmittance values were evaluated in white matter regions that have a relatively homogeneous tissue composition and predominantly flat fiber structures (areas surrounded in green) or steep fiber structures (areas surrounded in yellow). Regions belonging to the same fiber structure were evaluated together. The approximate orientation of the fibers is known from the anatomy of the rat and vervet brain as described in the atlases, and was confirmed by the retardation images shown below the transmittance images in Fig. 1: regions with flat fibers show larger retardation values than regions with steep fibers. The mean transmittance values and the standard deviation for the evaluated green and yellow regions can be found in Supplementary Tab. 1: In regions with flat fiber structures, the mean transmittance values are larger ( $\overline{I_{T,N}} \in [0.18, 0.33]$ ) than in regions with steep fiber structures ( $\overline{I_{T,N}} \in [0.08, 0.15]$ ). Two regions with flat and steep fiber structures which show large and small transmittance values in one section plane (coronal or sagittal), respectively, show the opposite behavior in the corresponding perpendicular section plane. The difference is especially large when comparing the transmittance values of the *corpus callosum (cc)* and the *cingulum (cg)*: In the coronal brain sections, the transmittance values of the cingulum are about 55–67% less than the transmittance values of the corpus callosum. In the sagittal brain sections, the transmittance values of the corpus callosum are about 50–54% less than the transmittance values of the cingulum. Rat and vervet brains show a similar behavior.

In Supplementary Fig. 7, we demonstrate that images obtained from standard transmission microscopy (using unpolarized light) show similar effects.

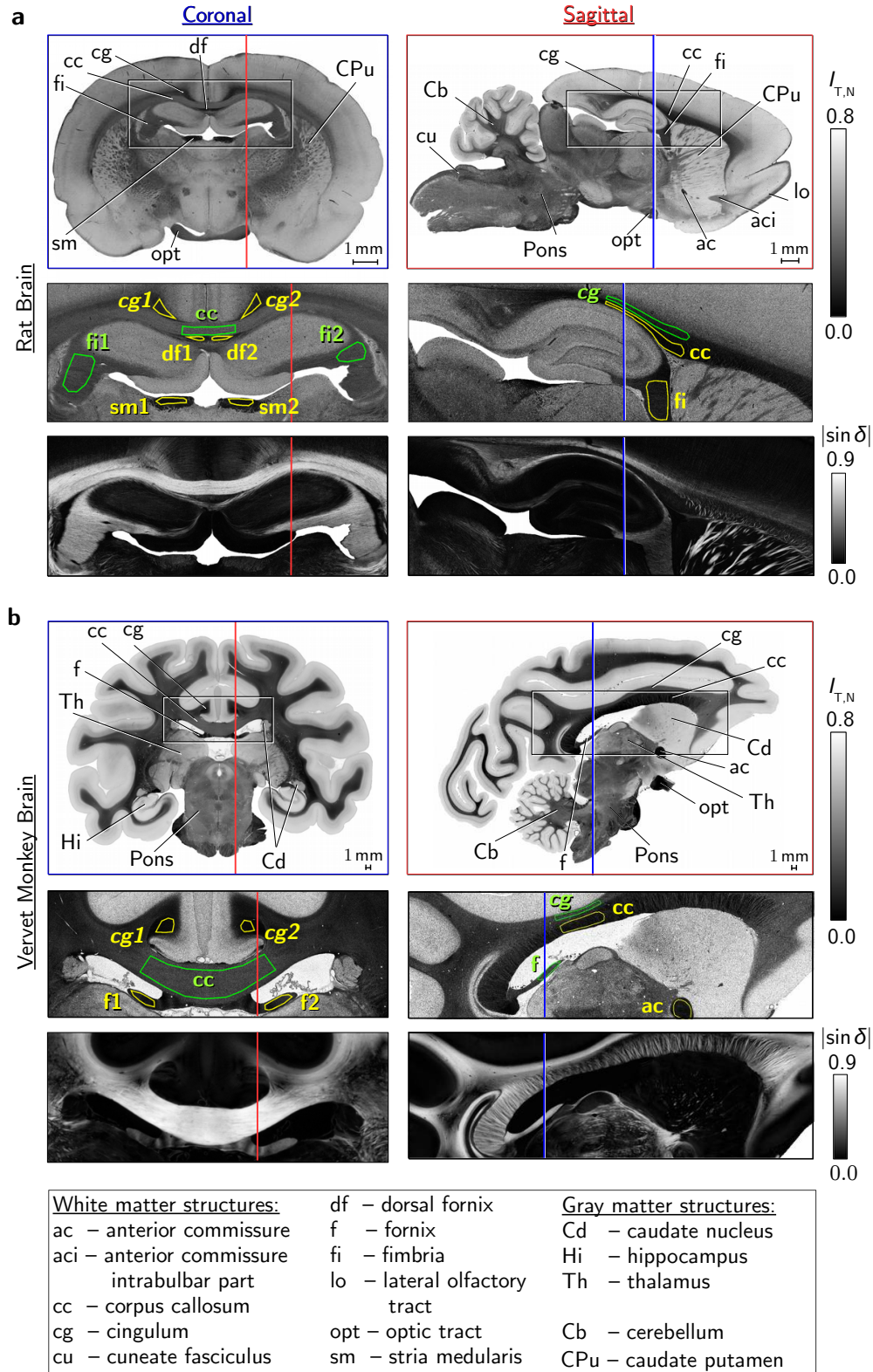


**Fig. 1.** Transmittance and retardation images of coronal and sagittal brain sections for a rat (a) and a vervet monkey (b). The coronal (sagittal) section planes are indicated by blue (red) lines in the respective other brain section for reference. Selected anatomical structures are labeled. The upper two rows show the normalized transmittance images  $I_{T,N}$ , the third row shows the retardation images  $|\sin \delta|$  obtained from 3D-PLI measurements with  $1.33 \mu\text{m}$  pixel size (see [Methods](#)). The images in the first row show the whole brain section, the images in the second and third row show an enlarged view of the region surrounded by the rectangle. The selected regions in yellow (green) belong to steep (flat) fiber structures, which appear dark (bright) in the transmittance and retardation images.

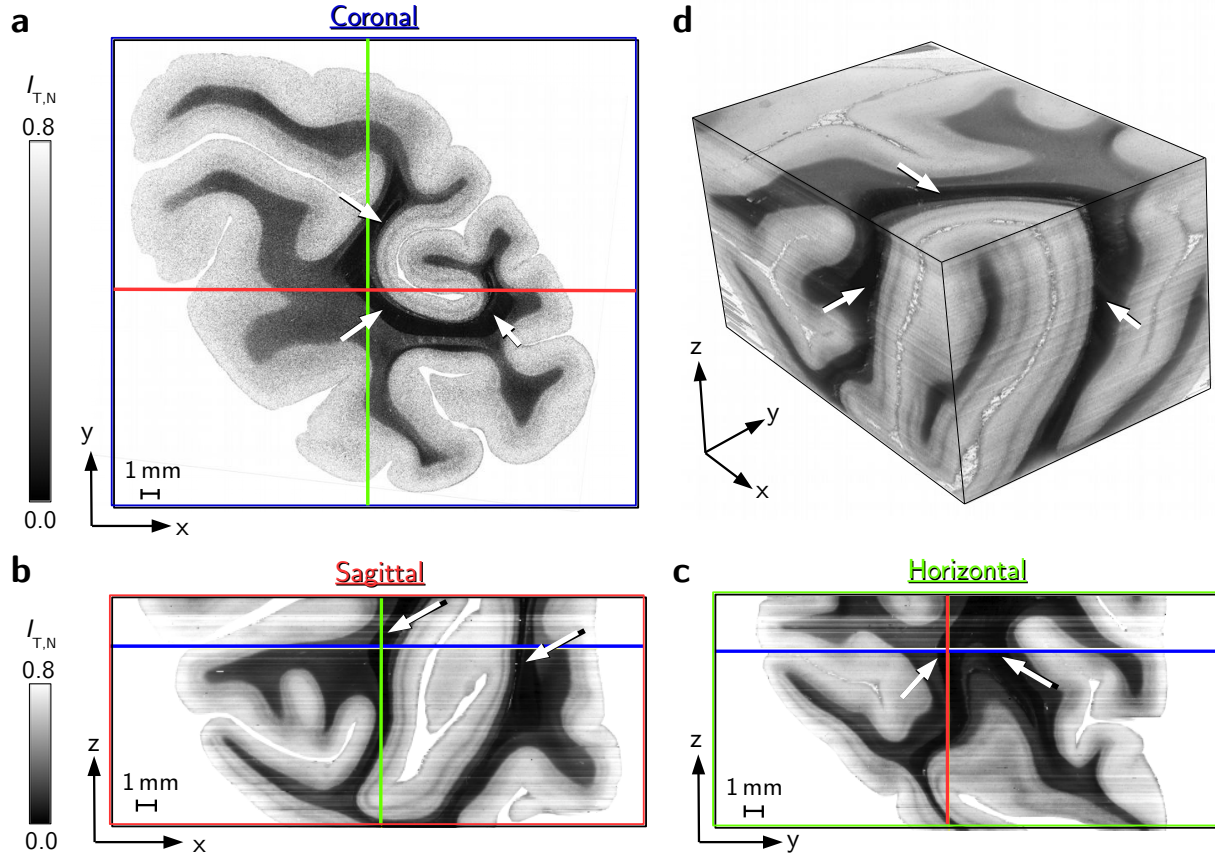


**Fig. 2.** 3D-reconstructed normalized transmittance images ( $I_{T,N}$ ) of the right hemisphere of a vervet monkey brain (234 consecutive brain sections from the occipital lobe). The brain was cut along the coronal plane ( $xy$ -plane), the resulting brain sections were registered onto each other from posterior to anterior (in the positive  $z$ -direction). **a-c** 3D-volume shown along the coronal ( $xy$ ), sagittal ( $xz$ ), and horizontal ( $yz$ ) plane. The colored lines indicate the position of the displayed  $xy$ -,  $xz$ -, and  $yz$ -planes. **d** Detail of the 3D-volume. The white arrows point to the *sagittal stratum* – a white matter structure with fibers that are mostly oriented perpendicularly to the image plane (along the  $z$ -direction) and which appears much darker in the transmittance images than the surrounding tissue.

The observation that steep fibers show lower transmittance values than flat fibers is consistent across consecutive brain sections. Figure 2 shows the 3D-reconstructed transmittance images of one vervet hemisphere along the coronal, sagittal, and horizontal plane (a-c) and a detail of the 3D-volume (d). The white arrows point to the *sagittal stratum* – a white matter structure that runs mostly perpendicularly to the image plane (along the  $z$ -direction), as can be seen in the sagittal and horizontal planes. The fiber structure appears much darker in the transmittance images than the surrounding tissue.

In a further study, we evaluated the transmittance contrast ( $C \equiv (I_{T,\max} - I_{T,\min}) / (I_{T,\max} + I_{T,\min})$ ) between striatum fibers and surrounding tissue in the caudate putamen of a rat brain (see Supplementary Fig. 8). The inclination angles of the nerve fibers were estimated by evaluating the fiber orientations in mutually orthogonal section planes. The contrast between the peak transmittance values of flat fiber bundles and surrounding tissue is much lower ( $5^\circ \leq \alpha \leq 60^\circ$ :  $C \approx 14\text{--}20\%$ ) than the corresponding contrast for steep fiber bundles ( $45^\circ \leq \alpha \leq 85^\circ$ :  $C \approx 62\%$ ). Assuming that the surrounding tissue is mostly composed of gray matter and that the transmittance is mostly independent of the fiber orientation, this demonstrates that the

transmittance values for steep fibers are significantly lower than for flat fibers.

Finally, to quantify how the transmittance depends on the fiber inclination, the caudate putamen of a coronal mouse brain section was measured with 3D-PLI and TPFM to determine the inclination angles of the striatum fiber bundles (see Supplementary Fig. 9). The scatter plot in Fig. 3d shows the normalized transmittance values plotted against the determined inclination angles for 40 evaluated fiber bundles. Although the values are broadly distributed, the scatter plot shows a clear tendency towards a decrease in transmittance with increasing fiber inclination. The values shown in red belong to regions with lower fiber densities which might lead to overestimated transmittance values. However, the decrease in transmittance is also observed in regions with maximum fiber density (values in blue): while the mean transmittance values for flat fibers ( $\alpha < 50^\circ$ ) reach larger values ( $0.1 < \overline{I_{T,N}} < 0.2$ ), the mean transmittance values for steep fibers ( $\alpha > 60^\circ$ ) are small ( $\overline{I_{T,N}} < 0.05$ ).

All our experimental studies show that the transmittance of brain tissue decreases significantly (by more than 50%) with increasing inclination angle of the enclosed nerve fibers.

**Simulated transmittance of inclined fiber bundles.** To model and better understand the observed inclination dependence of the transmittance, we generated a *bundle of densely grown fibers* (see Fig. 3a and Supplementary Note 1) for different inclination angles  $\alpha = \{0^\circ, 10^\circ, \dots, 90^\circ\}$ , and computed the transmittance from a simulated 3D-PLI measurement by means of FDTD simulations (see Methods, Supplementary Note 3). The bundle consists of 700 fibers with diameters between  $1 \mu\text{m}$  and  $1.6 \mu\text{m}$  and fills a volume of  $30 \times 30 \times 30 \mu\text{m}^3$ .

Figure 3b shows the resulting scattering patterns (i. e. the in-

tensity per wave vector) of light transmitted through the sample for inclination angles  $\alpha = 0^\circ$  and  $70^\circ$ . The transmittance images and scattering patterns for all inclination angles can be found in Supplementary Fig. 11b,c. For flat fibers ( $\alpha < 45^\circ$ ), the light is mostly scattered under angles perpendicular to the principal axis of the fiber bundle (i. e. along the y-axis). For intermediate inclination angles, the light is scattered more and more in the direction of the fibers (i. e. in the positive x-direction). For an inclination angle of  $70^\circ$ , the light is broadly scattered in almost all directions.

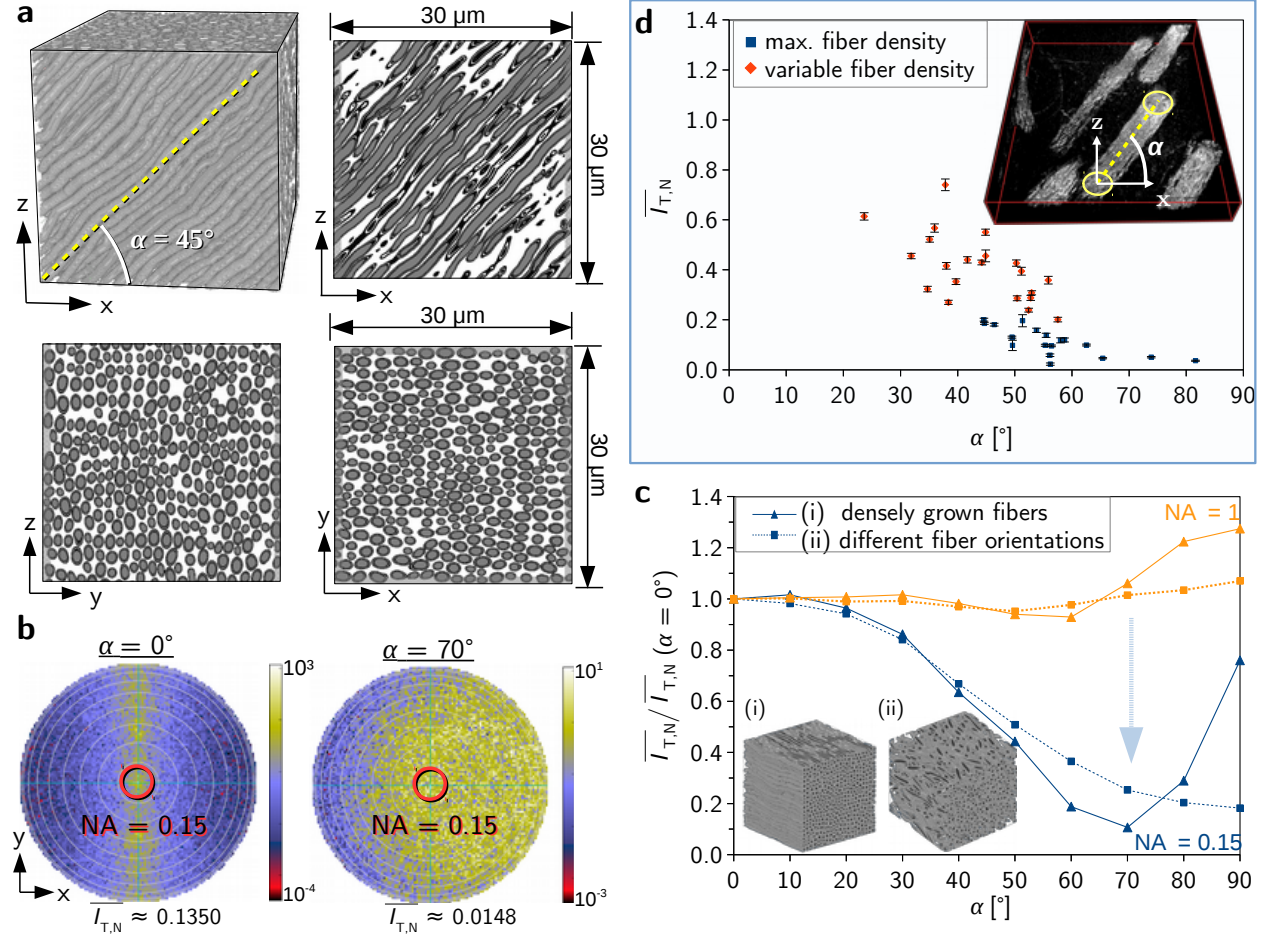


**Fig. 3.** Transmittance of inclined fiber bundles. **a** 3D view and cross-sections through mid-planes for the bundle of densely grown fibers shown exemplary for an inclination angle  $\alpha = 45^\circ$ . The bundle consists of 700 fibers with diameters between  $1 \mu\text{m}$  and  $1.6 \mu\text{m}$  and fills a volume of  $30 \times 30 \times 30 \mu\text{m}^3$  (see Supplementary Note 1). **b** Light-scattering patterns obtained from 3D-PLI simulations for the bundle of densely grown fibers with  $\alpha = 0^\circ$  and  $70^\circ$ . To compute the mean normalized transmittance values  $\overline{I_{T,N}}$  for the numerical aperture of the imaging system ( $NA = 0.15$ ), only wave vector angles  $\theta_k \leq 8.6^\circ$  were considered (see red circles). The white circles represent steps of  $\Delta\theta_k = 10^\circ$ . **c** Simulated transmittance curves (mean transmittance  $\overline{I_{T,N}}$  vs. inclination  $\alpha$ ) for the bundle of densely grown fibers (i) and for a bundle with broad fiber orientation distribution (ii) for  $NA = 1$  (orange curves) and  $NA = 0.15$  (blue curves). The transmittance curves were normalized by the mean transmittance values of the horizontal bundles, respectively. The simulations were performed as described in Methods (using a normally incident plane wave with  $550 \text{ nm}$  wavelength and simulations parameters specified in Supplementary Tab. 2). **d** Mean normalized transmittance values  $\overline{I_{T,N}}$  plotted against the nerve fiber inclination angles  $\alpha$  determined from 3D-PLI and TPFM measurements of mouse striatum fibers (see Supplementary Fig. 9). The values in blue belong to regions with similar (maximum) fiber density, the values in red belong to regions with variable fiber density in which the transmittance might be overestimated. The error bars indicate the standard error of the mean for the evaluated transmittance values. Both experimental and simulated data show that the transmittance decreases with increasing fiber inclination.

Due to the numerical aperture of the employed imaging system ( $NA \approx 0.15$ , see [Methods](#)), light scattered under angles larger than  $\arcsin(NA) \approx 8.6^\circ$  does not contribute to the measured transmittance images. To study the effect of the finite aperture on the measured transmittance values, we simulated the imaging system without aperture ( $NA = 1$ ) considering light scattered under all angles, and with aperture ( $NA = 0.15$ ) considering only light scattered under angles  $< 8.6^\circ$  (indicated by the red circles in [Fig. 3b](#)).

[Figure 3c](#) shows the resulting transmittance curves (mean values of the simulated transmittance images plotted against the inclination angles of the fiber bundle) for  $NA = 1$  (orange curves) and  $NA = 0.15$  (blue curves). The solid curves were obtained from the bundle of densely grown fibers (i) which has similar fiber orientations (the mode angle difference between the local fiber orientation vectors and the predominant orientation of the fiber bundle is less than  $10^\circ$ ). The dashed curves were obtained for a *bundle with broad fiber orientation distribution* (ii) which contains many different fiber orientations (the mode angle difference is about  $25^\circ$ , see [Supplementary Note 1](#)). To enable a better comparison between horizontal fiber bundles ( $\alpha = 0^\circ$ ) and vertical fiber bundles ( $\alpha = 90^\circ$ ), all curves were divided by the mean transmittance value of the horizontal bundle, respectively. [Supplementary Fig. 12a,c](#) shows the (normalized) transmittance curves in separate figures.

For  $NA = 1$ , the transmittance for steep fibers is similar to or even slightly larger than the transmittance for flat fibers. For  $NA = 0.15$ , the transmittance decreases significantly between  $\alpha = 30^\circ$  and  $\alpha = 70^\circ$ . This implies that the observed decrease in transmittance is caused by the finite numerical aperture of the imaging system: for steep fibers, the light is scattered almost uniformly in all possible directions (cf. [Fig. 3b](#) for  $\alpha = 70^\circ$ ) so that the detected transmitted light intensity becomes minimal. In simulation studies with polarized light, we could show that the decrease in transmittance is independent of the direction of polarization (see [Supplementary Fig. 18a](#)) which suggests that the decrease is caused by isotropic (not by anisotropic) scattering of light.

While the transmittance for the bundle of densely grown fibers becomes minimal at  $\alpha = 70^\circ$  for  $NA = 0.15$  (the transmittance is 90 % less than the transmittance for the horizontal bundle) and the transmittance for vertical fibers ( $\alpha = 90^\circ$ ) is only about 25 % less than for horizontal fibers ( $\alpha = 0^\circ$ ), the transmittance for the bundle with broad fiber orientation distribution decreases monotonically with increasing fiber inclination angle and becomes minimal for vertical fibers (the transmittance for vertical fibers is more than 80 % less than for horizontal fibers). Due to the broad fiber orientation distribution, the vertical bundle contains many fibers with inclinations between  $60^\circ$  and  $70^\circ$ , which explains why the minimum transmittance is shifted to larger inclination angles.

Especially for the bundle with broad fiber orientation distribution, the simulated transmittance curves ([Fig. 3c](#)) show a similar behavior as the measured transmittance values in the scatter plot ([Fig. 3d](#)).

The brain sections used for the 3D-PLI measurements are embedded in glycerin solution (see [Methods](#)). With increasing time after tissue embedding, the brain sections become more and more transparent, i. e. the transmittance increases (see [Supplementary Fig. 13](#)). To enable optimal transmittance contrasts,

the brain sections were therefore measured directly after embedding and the simulations were performed assuming that the refractive indices of the nerve fibers correspond to given literature values (see [Methods](#) and [Supplementary Note 2](#)). With increasing time after tissue embedding, the glycerin solution presumably soaks into the myelin sheaths which surround the axons. As the glycerin solution has a lower refractive index than the myelin lipids, the effective refractive index of the myelin sheaths is expected to decrease. [Supplementary Fig. 12b](#) shows the resulting transmittance curves for the bundle of densely grown fibers with a reduced myelin refractive index: the mean transmittance for steep fibers ( $\alpha = 70\text{--}80^\circ$ ) is only about 30 % less than the mean transmittance for horizontal fibers, the absolute transmittance values are larger than in [Fig. 12a](#). This corresponds to the experimental observation that the transmittance increases with increasing time after tissue embedding.

**Simulated transmittance of crossing fiber bundles.** As our previous simulation studies have shown that the transmittance strongly depends on the fiber inclination, the transmittance could be used to distinguish between horizontal  $90^\circ$ -crossing and vertical fibers which can to date not be distinguished in standard 3D-PLI measurements. Therefore, we simulated the transmittance of horizontal crossing fibers for different crossing angles and compared the results to the transmittance of steep fiber structures.

The horizontal crossing fibers were generated as separate and interwoven fiber bundles (see [Supplementary Note 1](#) and [Fig. 14a,b](#)) with different crossing angles  $\chi = \{0^\circ, 15^\circ, \dots, 90^\circ\}$ . [Figure 4a](#) shows the scattering patterns and the mean transmittance values for  $NA = 0.15$  and  $\chi = \{90^\circ, 60^\circ, 30^\circ\}$ . The scattering patterns of separate and interwoven crossing fiber bundles look similar for all crossing angles. The underlying fiber structure, i. e. the crossing angle of the fiber bundles, is clearly visible in all scattering patterns. The mean transmittance values for the interwoven fiber bundles are up to 13 % larger than those for the separate fiber bundles and in both cases mostly independent of the crossing angle.

[Figure 4b](#) shows the scattering pattern for three mutually orthogonal, interwoven fiber bundles. The fiber configuration is similar to the horizontal  $90^\circ$ -crossing, interwoven fiber bundles, but one third of the fibers is oriented in the z-direction (see [Supplementary Note 1](#) and [Fig. 14c](#)). This configuration leads to lower transmittance values than the horizontal crossing fibers.

[Figure 4c](#) shows the scattering pattern for a vertical fiber bundle (bundle with broad fiber orientation distribution and  $\alpha = 90^\circ$ , cf. [Fig. 3c\(ii\)](#)). The scattering pattern looks clearly different from the scattering pattern of the horizontal crossing fibers and the mean transmittance is much lower.

[Figure 4d](#) shows the mean transmittance values of the different fiber bundles for  $NA = 0.15$  plotted against the crossing angle  $\chi$  (in the case of horizontal crossing fibers). For better comparison, the values were divided by the mean transmittance value of the corresponding horizontal fiber bundle (with  $\chi = 0^\circ$ ), respectively. The solid curves belong to the horizontal crossing fibers (separate and interwoven bundles), the densely dotted lines belong to fiber constellations that contain vertical or steep fibers: the bundle of densely grown fibers for  $\alpha = 90^\circ$  and  $70^\circ$ , the mutually orthogonal fiber bundles, and the bundle with broad fiber orientation distribution for  $\alpha = 90^\circ$ .

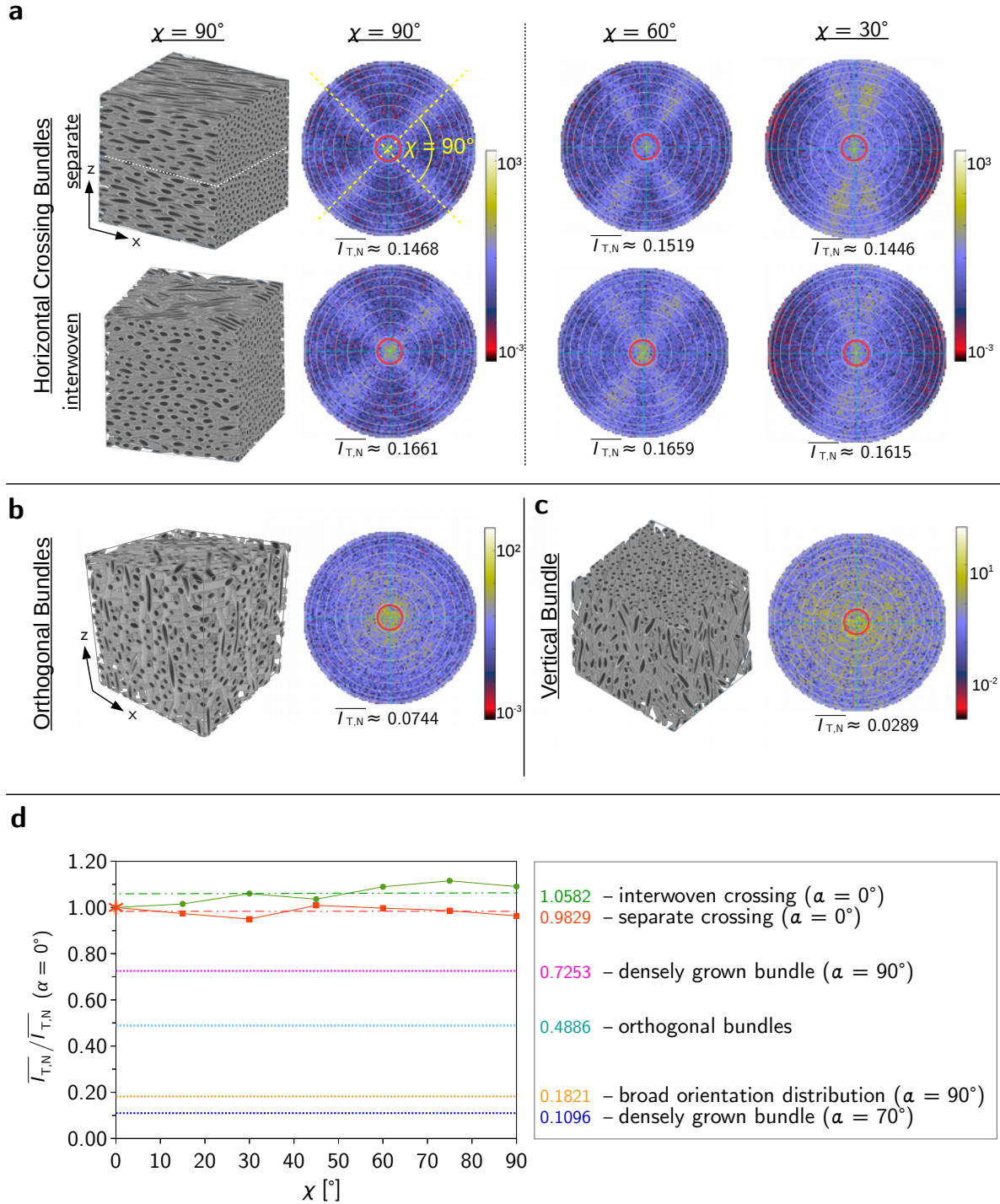


**Fig. 4.** Simulated transmittance of crossing fibers. **a–c** 3D views and light-scattering patterns for (a) horizontal crossing fibers (separate and interwoven bundles, cf. Supplementary Fig. 14a,b) with crossing angle  $\chi$ , (b) three mutually orthogonal, interwoven fiber bundles (cf. Supplementary Fig. 14c), and (c) a vertical fiber bundle with broad fiber orientation distribution (cf. Fig. 3c(ii)). The mean normalized transmittance values  $\overline{I_{T,N}}$  were computed from a simulated 3D-PLI measurement (with numerical aperture  $\text{NA} = 0.15$ ). The simulations were performed as described in [Methods](#) (using a normally incident plane wave with 550 nm wavelength and simulations parameters specified in Supplementary Tab. 2). **d** Mean transmittance values for different crossing angles  $\chi$  shown for in-plane crossing (solid curves) and out-of-plane fiber structures (densely dotted curves). For better comparison, the values were divided by the mean transmittance value of the corresponding horizontal fiber bundle with  $\chi = 0^\circ$ . Apart from the fiber configurations shown in this figure, the mean transmittance values are also displayed for the bundle of densely grown fibers (see Fig. 3c) for  $\alpha = 70^\circ$  and  $90^\circ$ . While the scattering patterns show the crossing angles of in-plane crossing fibers, the mean transmittance is mostly independent of the crossing angle and larger than the mean transmittance of out-of-plane fiber structures.

The transmittance curves of horizontal crossing fibers are similar for separate and interwoven fiber bundles. While the mean transmittance of the separate crossing fibers corresponds more or less to the mean transmittance of the horizontal fiber bundle with  $\chi = 0^\circ$ , the transmittance values of the interwoven crossing fibers slightly increase with increasing crossing angle (by max. 11 %).

For all simulated fiber bundles that contain vertical or steep fibers, the mean transmittance values (densely dotted lines) are more than 26 % less than for the horizontal crossing fibers (solid lines). For interwoven crossing fibers, the transmittance value is reduced by more than one half when the horizontal crossing fibers are combined with a vertical fiber bundle (orthogonal bundles). For the vertical bundle with broad fiber orientation distribution and the steep bundle of densely grown fibers (with  $\alpha = 70^\circ$ ), the difference between the transmittance values is especially large: the transmittance is about 80–90 % less than for the horizontal crossing fibers.

Our simulations of crossing fibers have shown that the transmittance for horizontal fibers is mostly independent of the crossing angle and much larger than the transmittance for vertical fibers, which suggests that the transmittance values can be used to distinguish between horizontal crossing and vertical fibers, and to detect vertical fibers within fiber crossings.

**Combination of experimental and simulation studies.** To verify our prediction that the transmittance of in-plane fibers does not depend on the crossing angle, we investigated the optic chiasm of a hooded seal [4] – a region that contains fibers with crossing angles of about  $90^\circ$  in the image plane (see Fig. 5).

While the retardation values in the region with crossing fibers (region B) are broadly distributed (the birefringence signals of crossing fibers cancel out), the transmittance values in this region show a similar distribution as in a region with mostly parallel fibers (region A), see histograms in Fig. 5d.

The peak transmittance value of region B is slightly lower than in region A because the number of fibers in the crossing region (two crossing bundles) is larger than in the region with parallel fibers (one bundle). Thus, the transmittance depends on the tissue density, but not on the crossing angles of the fibers – as predicted by the simulations.

To demonstrate that the transmittance can be used to classify regions with small birefringence signals (i. e. small retardation values) into regions with in-plane crossing fibers, regions with steep fibers, and regions with low fiber density, the predictions obtained from the simulation studies were applied to experimental data (see Fig. 6).

As the transmittance depends on absorption, the region with maximum absorption was determined as a reference: The retardance  $\delta$  of brain tissue increases with decreasing fiber inclination  $\alpha$  and with increasing thickness  $d$  of birefringent tissue components ( $\delta \propto d \Delta n \cos^2 \alpha$ , where  $\Delta n$  is the birefringence of the tissue). Assuming that a brain section contains all possible nerve fiber configurations, the region with maximum retardation signal  $|\sin \delta|_{\max}$  (orange ellipse) is therefore expected to contain mostly horizontal parallel fibers ( $\alpha \approx 0^\circ$ ) with a high fiber density (max.  $d \Delta n$ ) and thus to cause a maximum of absorption. Regions with even lower transmittance values are accordingly expected to contain steep (out-of-plane) fibers which increase the scattering and thus the attenuation of light.

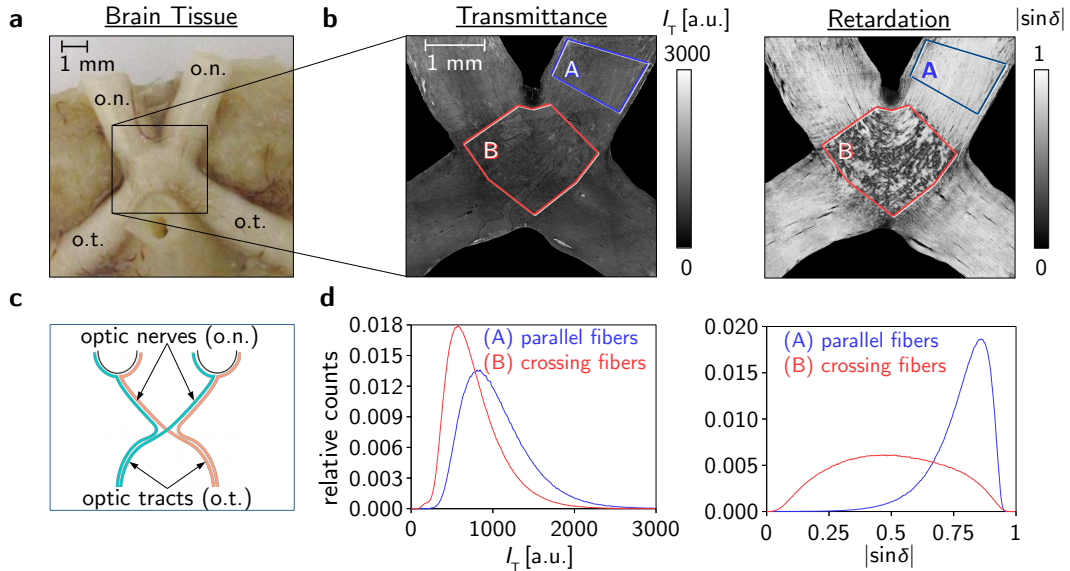


**Fig. 5.** Crossing fibers in the optic chiasm of a hooded seal: **a** brain tissue before sectioning, **b** unnormalized transmittance and retardation images of the middle brain section obtained from 3D-PLI measurements with  $1.33 \mu\text{m}$  pixel size (see Methods), **c** schematic drawing of the optic chiasm consisting of optic tracts (o.t.) and optic nerves (o.n.), **d** normalized histograms of the transmittance images ( $I_T$ ) and retardation images ( $|\sin \delta|$ ) for a region with mostly parallel fibers (blue) and a region with nearly  $90^\circ$ -crossing fibers (red). The transmittance depends on the tissue density, but not on the crossing angles of the fibers like the retardation. More information about the sample can be found in DOHMEN *et al.* [4] (Figs. a and c were adapted from Figs. 1B and 5B0).

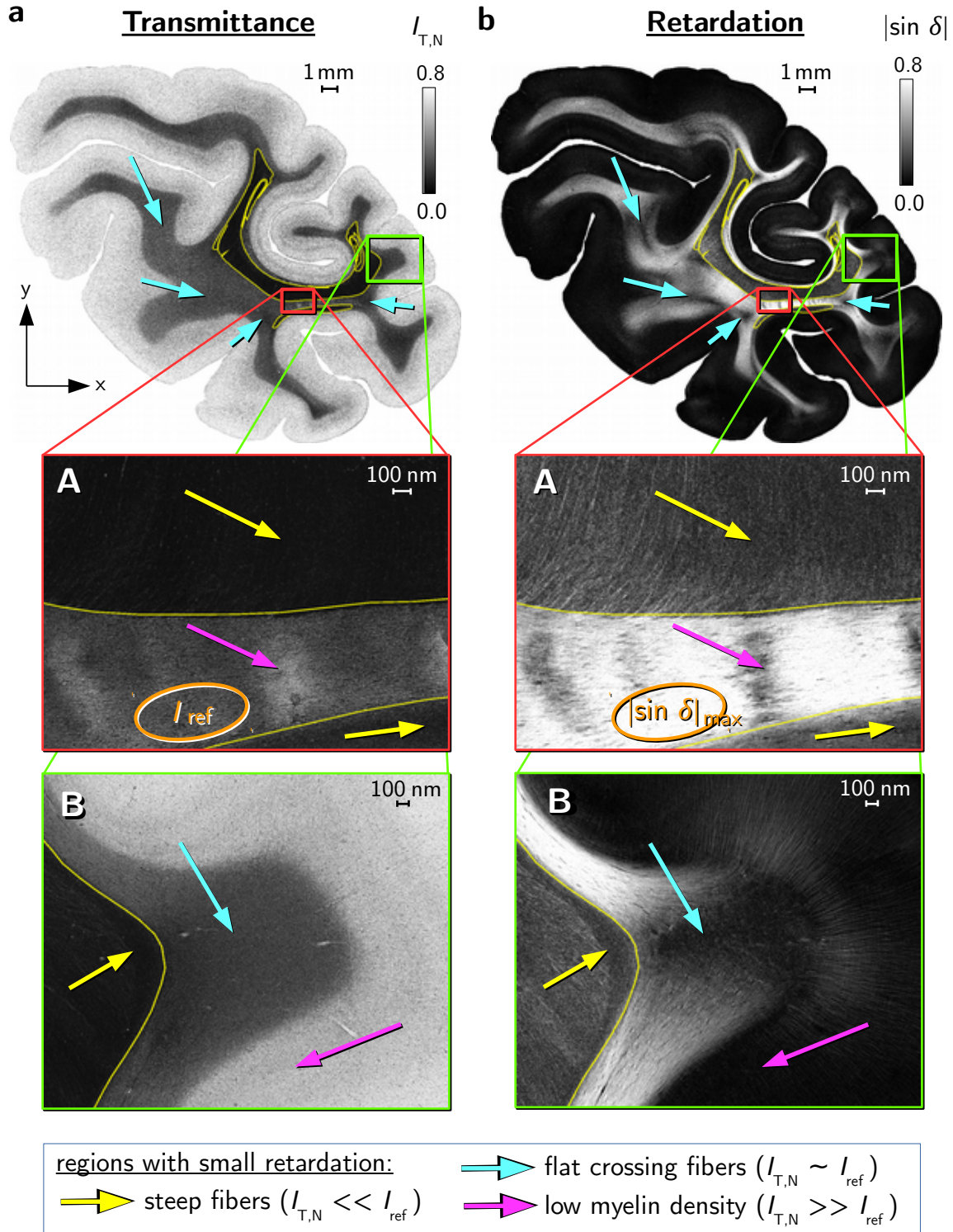


**Fig. 6.** Combined analysis of transmittance and retardation images allowing to distinguish between brain regions with in-plane crossing fibers and out-of-plane fibers. The figure shows the normalized transmittance image ( $I_{T,N}$ ) and the retardation image ( $|\sin \delta|$ ) of a coronal section through the right hemisphere of a vervet brain (cf. Fig. 2a). The transmittance in the region with maximum retardation (orange ellipse) is used as a threshold value ( $I_{ref} \equiv I_{T,N}(|\sin \delta|_{max})$ ). Regions with small retardation values and notably lower transmittance values ( $I_{T,N} \ll I_{ref}$ , yellow arrows and regions surrounded by a yellow line) are expected to contain steep (out-of-plane) fibers. Regions with small retardation values and similar transmittance values ( $I_{T,N} \sim I_{ref}$ , cyan arrows) are expected to contain flat (in-plane) crossing fibers. Regions with small retardation values and larger transmittance values ( $I_{T,N} > I_{ref}$ , magenta arrows) belong to regions with low fiber density, i. e. regions with a large amount of unmyelinated axons or surrounding tissue.

By comparing the normalized transmittance values ( $I_{T,N}$ ) of regions with small retardation values to the transmittance of the region with maximum retardation ( $I_{ref} \equiv I_{T,N}(|\sin \delta|_{max})$ ), the regions can be classified into three categories (see Fig. 6):

1.  $I_{T,N} \ll I_{ref}$ : regions with notably lower transmittance values are expected to contain steep (out-of-plane) fibers (see yellow arrows and regions surrounded by a yellow line),
2.  $I_{T,N} \sim I_{ref}$ : regions with similar transmittance values are expected to contain flat (in-plane) crossing fibers (see cyan arrows),
3.  $I_{T,N} \gg I_{ref}$ : regions with notably larger transmittance values are expected to have a lower fiber density (see magenta arrows).

For regions with slightly lower or larger transmittance values, an unambiguous classification is not possible. Provided that the region with maximum retardation has the largest tissue absorption, lower transmittance values can only be caused by steep fibers. Similar transmittance values, however, could also be caused by a small number of steep fibers, and larger transmittance values could be caused by a small number of in-plane crossing fibers (or a smaller number of steep fibers). A classification by means of retardation and transmittance values can therefore only serve as an indication of the underlying fiber structure and should always be considered in addition to individual tissue characteristics. As the transmittance depends on the tissue preparation, the combined analysis of transmittance and retardation should only be performed section-wise.

Brain atlases and 3D-reconstructed images (cf. Fig. 2) validate the classification of regions in Fig. 6 (coronal vervet section).

## DISCUSSION

Our experimental studies on various brain sections (see Figs. 1, 2, 8 and 9) have shown that the polarization-independent transmitted light intensity (transmittance) significantly decreases with increasing out-of-plane inclination angle of the enclosed nerve fibers (by more than 50%). Using finite-difference time-domain (FDTD) simulations, we could successfully model this effect and show that the decrease in transmittance is caused by polarization-independent (isotropic) light scattering and by the finite numerical aperture of the imaging system (see Fig. 3). Polarization-dependent light scattering which leads to diattenuation cannot explain the observed transmittance effect because the diattenuation of brain tissue was shown to be small [5].

Furthermore, we could demonstrate that the increasing transparency of aging brain tissue samples (see Supplementary Fig. 13) is caused by the fact that the embedding solution soaks into the nerve myelin sheaths which leads to an equalization of the effective refractive indices and thus to reduced scattering.

More importantly, our simulations indicated that the transmittance of flat fiber structures does not depend on the crossing angle between the fibers (see Fig. 4d). With 3D-Polarized Light Imaging (3D-PLI), it is generally not possible to distinguish between regions with horizontal crossing fibers, regions with vertical fibers, and regions with a low fiber density because they all yield low birefringence signals. Applying the predictions of the simulation studies to experimental data, we could

demonstrate that a combined analysis of transmittance and retardation (strength of the birefringence signal) enables to distinguish between these regions. Our simulations also revealed that the transmittance can be used to detect vertical fibers in regions with horizontal crossing fibers, which is not possible with current techniques.

The transmittance effects have been demonstrated to depend mostly on (isotropic) scattering and not on the polarization of light – conventional transmission microscopy images show similar effects (see Supplementary Fig. 7). Thus, our results are also relevant for other microscopy techniques that use unpolarized light.

Finally, the simulations of the transmittance revealed that the scattering patterns provide unique information about the underlying fiber structure and could for example be used to determine the crossing angle of in-plane crossing fibers.

The FDTD simulations proved to be a valuable and reliable tool in many aspects: they allow to better understand the interaction of polarized light with brain tissue, to find explanations for the observed transmittance effects, to make general predictions, and to improve the measurement procedure and analysis. In contrast to previous top-down simulation approaches of 3D-PLI that model the optical properties of the nerve fibers by series of Jones matrices (*simPLI* [3, 4]), the FDTD simulations solve Maxwell’s equations and allow to model more complex effects like the scattering of light, but they are computationally much more expensive.

In future studies, more experimental data should be generated to obtain better statistics and to enable a quantitative description of the observed effects. This would e.g. allow to include the inclination dependence of the transmittance in the correction of the measured birefringence signals [14].

A more detailed knowledge of the structure and the optical properties of brain tissue would help to create more realistic fiber configurations and enable an even better comparison between simulation and experiment.

As the scattering patterns turned out to provide interesting information about the underlying fiber structure, future simulations should study the scattering patterns of various fiber structures to find out whether the patterns can for example be used to distinguish between crossing (X) and kissing ( $\supset$ ) fibers or between interwoven and separate crossing fibers. In addition, measurement techniques should be explored that enable to measure the scattering pattern of the brain sections.

The overall aim of future work should be to bring theory, simulation, and experiment together and to integrate the simulation results into the image analysis of 3D-PLI. As a first step, the transmittance should become part of the standard signal analysis to enable the distinction between brain regions with horizontal crossing and vertical fibers. The combined analysis of transmittance and retardation images should also be applied to past 3D-PLI measurements in order to validate and – if necessary – correct the reconstructed fiber orientations.

## METHODS

**Preparation of brain sections.** The experimental studies were performed on healthy brains from different species: vervet monkey (African green monkey: *Chlorocebus aethiops sabaeus*, male, between one and two years old), rat (*Wistar*, male, three months old), mouse

(C57BL/6, male, six months old), and hooded seal [4].

All animal procedures were approved by the institutional animal welfare committee at Forschungszentrum Jülich GmbH, Germany, and are in accordance with European Union (National Institutes of Health) guidelines for the use and care of laboratory animals.

The brains were removed from the skull within 24 hours after death, immersed in a buffered solution of 4 % formaldehyde for several weeks, immersed for several days in solutions of 10 % and 20 % glycerin combined with 2 % Dimethyl sulfoxide for cryoprotection, dipped in cooled isopentane for several minutes, and deeply frozen. The frozen brains were cut with a cryostat microtome (*Leica Microsystems*, Germany) at a temperature of  $-30^\circ\text{C}$  into sections of  $60\ \mu\text{m}$ . The brain sections were mounted on cooled glass slides, embedded in 20 % glycerin solution, covered by a cover glass, sealed with lacquer, and weighted for several hours to prevent the development of air bubbles. The sections were measured one day after embedding to obtain optimal transmittance images.

**3D-PLI measurements.** The brain sections were measured with a high-resolution *Polarizing Microscope (PM)* manufactured by *Taorad GmbH*, Germany. The microscope has been used in previous 3D-PLI studies to measure the three-dimensional nerve fiber orientations at high resolution [1, 2, 15, 16]. It consists of a green LED light source ( $\lambda = (550 \pm 5)\ \text{nm}$ ), a rotatable linear polarizer, a specimen stage, a circular analyzer (quarter-wave retarder combined with linear polarizer), and a CCD camera (monochrome *RETIGA-4000R* camera by *QImaging* with *Kodak KAI-04022-ABA* image sensor) which records an image for each rotation angle  $\rho = \{0^\circ, 10^\circ, \dots, 170^\circ\}$  of the polarizer. The microscope is equipped with a motorized specimen stage which performs a translational scan of the brain section in tiles of  $2.7 \times 2.7\ \text{mm}^2$ . To allow for stitching, the tiles were measured with an overlap of 30 % on all sides. The objective lens (*Nikon TL Plan Fluor EPI P 5x*) has a  $5\times$  magnification and a numerical aperture of 0.15. The resolution in object space is about  $1.33\ \mu\text{m}/\text{px}$ .

The transmittance and retardation images were computed as described in *AXER et al.* [1, 2] by performing a discrete harmonic Fourier analysis on the measured light intensities per image pixel ( $I(\rho) = a_0 + a_2 \cos(2\rho) + b_2 \sin(2\rho)$ ): the transmittance corresponds to the average over all 18 images and was computed from the Fourier coefficient of order zero ( $I_T = 2a_0$ ), the retardation corresponds to the amplitude of the intensity signal and was computed from the Fourier coefficients of order two ( $|\sin \delta| = (a_2^2 + b_2^2)^{1/2}/a_0$ ), where  $\delta$  is the phase shift induced by the birefringent brain tissue. The transmittance images were normalized by the transmittance image measured without sample, yielding  $I_{T,N}$ .

**3D-reconstruction of transmittance images.** The reconstructed volume in Fig. 2 consists of 234 consecutive brain sections obtained from the right hemisphere of a vervet brain (occipital lobe). The brain was cut along the coronal plane (xy-plane), the brain sections were registered onto each other from posterior to anterior (in the positive z-direction). The registration was performed using in-house developed software tools based on the software packages *ITK*, *elastix*, and *ANTs* [17–21] which perform linear and non-linear transformations. As undistorted reference volume, aligned blockface images were used: a picture of the brain block surface (*blockface image*) was taken every time before sectioning, a pattern of *ARTag markers* [22] was used to determine the position of the brain block in two-dimensional space [23].

**TPFM measurements.** The TPFM measurements [24, 25] were performed with a custom-made two-photon fluorescence microscope at the *European Laboratory for Non-Linear Spectroscopy (LENS)*, University of Florence, Italy. The microscope is equipped with a mode-locked titanium-sapphire laser with a wavelength of 800 nm which is coupled into a scanning system based on a pair of galvanometric mirrors. The laser is focused onto the sample by a water-immersion  $25\times$  objective lens (*LD LCI Plan-Apochromat 25x/0.8 Imm Corr DIC M27*). The lat-

eral displacement of the sample was realized by a motorized xy-stage (enabling tile-wise scanning of the sample). The axial displacement (along the z-axis) was realized by a closed-loop piezoelectric stage. The fluorescence signals were collected by two photomultiplier tubes, enabling to detect red and green fluorescence. The setup achieves a resolution of  $0.244 \times 0.244 \times 1\ \mu\text{m}^3$ . The sample was measured in tiles of  $250 \times 250\ \mu\text{m}^2$ , with an overlap of 10 % to allow for stitching.

To determine the inclination angle of the nerve fiber bundles in the measured brain section (see Supplementary Fig. 9), the cross-sections of the fiber bundles were determined in the first and the last slice of the TPFM image stack (see colored shapes in Supplementary Fig. 9d). For each fiber bundle, the inclination angle  $\alpha$  was computed from the mid points (xy-coordinates) of the corresponding cross-sections and from the thickness of the brain section in the z-direction (given by the number of slices in the TPFM image stack), cf. Supplementary Fig. 9c. The corresponding transmittance values were evaluated in the middle of the fiber bundles (see colored shapes in Supplementary Fig. 9b).

**Model of the simulated nerve fiber configurations.** The fiber configurations used for the FDTD simulations consist of about 700 fibers with uniformly distributed diameters between  $1.0\ \mu\text{m}$  and  $1.6\ \mu\text{m}$  and different fiber orientations. All fibers were generated in a volume of  $30 \times 30 \times 30\ \mu\text{m}^3$  without intersections. The generation of the fiber configurations is described in Supplementary Note 1 in more detail.

The generated fiber configurations differ in terms of their volume fraction (volume filled by fibers divided by the total volume size) and in terms of the mode angle difference between the local fiber orientation vectors and the predominant orientation of the fiber bundle. The bundle of densely grown fibers (Fig. 3a) has a volume fraction of about 60 %, the mode angle difference is less than  $10^\circ$ . For the bundle with broad fiber orientation distribution (Fig. 3c(ii)), the volume fraction is about 33 % and the mode angle difference about  $25^\circ$ . The volume fraction for the separate and interwoven crossing fiber bundles (Fig. 4a) is between 40 % and 50 %, depending on the crossing angle. The volume fraction for the mutually orthogonal, interwoven fiber bundles (Fig. 4b) is only about 32 %.

Each fiber with radius  $r$  was modeled by materials with different refractive indices  $n$ : an inner axon ( $r_{\text{ax}} = 0.65r$ ,  $n_{\text{ax}} = 1.35$ ) and a surrounding myelin sheath with thickness  $t_{\text{sheath}} = 0.35r$  that consists of two myelin (lipid) layers ( $t_m = 3/7t_{\text{sheath}}$ ,  $n_m = 1.47$ ) and a separating glycerin layer ( $t_g = 1/7t_{\text{sheath}}$ ,  $n_g = 1.37$ ). The surrounding medium was assumed to be homogeneous with a refractive index  $n_{\text{surr}} = n_g = 1.37$ , which corresponds to the refractive index of gray matter as well as to the refractive index of the surrounding glycerin solution. The motivation of the nerve fiber model is described in Supplementary Note 2 in more detail.

**FDTD algorithm.** The propagation of the polarized light wave through the sample was simulated by a massively parallel 3D Maxwell solver based on a conditionally stable finite-difference time-domain (FDTD) algorithm [26]. The algorithm computes the electromagnetic field components numerically by discretizing space and time and approximating Maxwell’s curl equations by finite differences: The discretization is realized with a cubic Yee grid [27] (each electric field component is surrounded by four magnetic field components and vice versa) and a leapfrog time-stepping scheme. The spatial and temporal derivatives in Maxwell’s curl equations are approximated by second-order central differences. For more details, see *MENZEL et al.* [28].

The simulations were performed with the software *TDME3D*<sup>TM</sup> [29, 30] – a massively parallel three-dimensional FDTD Maxwell Solver, Copyright *EMBD (European Marketing and Business Development BVBA)*. The software solves Maxwell’s equations for arbitrary-shaped objects that are illuminated by arbitrary incident plane waves and that consist of linear, isotropic, lossy materials with known permeability, permittivity, and conductivity. For the FDTD simulations, a combined algorithmic approach was used: In free space, Yee’s algorithm was applied. To compute the interaction of the light with brain tissue, an unconditionally stable *Lie-Trotter-Suzuki product formula ap-*

*proach* was used. This results in a computationally efficient but conditionally stable algorithm. For more information, see DE RAEDT [31]. The simulations were performed on the supercomputer *JUQUEEN* [32] at Forschungszentrum Jülich GmbH, Germany.

**Simulation parameters.** Supplementary Fig. 11a shows the geometry of the simulated fiber volume exemplary for the bundle of densely grown fibers (and  $\alpha = 45^\circ$ ). To account for the fact that the brain sections are embedded in glycerin solution,  $0.5\ \mu\text{m}$  thick layers of glycerin solution (with refractive index  $n_g = 1.37$ ) were added at the bottom and on top of the sample, yielding a total medium with dimensions  $30 \times 30 \times 31\ \mu\text{m}^3$ . The dimensions of the simulation box were chosen to be  $30 \times 30 \times 35\ \mu\text{m}^3$  to leave some space for light source and detection planes. The simulation volume was surrounded by uniaxial perfectly matched layer absorbing boundaries of  $1\ \mu\text{m}$  thickness, thick enough to prevent light from being reflected back into the simulation volume.

The different components of the sample were simulated as dielectrics with real refractive indices (cf. Supplementary Fig. 11a): axon (green,  $n_{ax} = 1.35$ ), myelin layers (blue,  $n_m = 1.47$ ), glycerin layer and surrounding medium (yellow,  $n_g = n_{surr} = 1.37$ ). As the absorption coefficients of brain tissue are small [6, 7], they were neglected in the simulations.

All simulations were performed for 200 time steps with Courant factor 0.8. The Yee mesh size was chosen to be  $\Delta = 25\ \text{nm}$ . This mesh size is just large enough to account for the double myelin layers of the fibers (the glycerin layer for fibers with  $1\ \mu\text{m}$  diameter is only  $25\ \text{nm}$  thick).

The light source was modeled as a plane monochromatic wave. All simulations were performed for normally incident and coherent light with left-handed circular polarization and a wavelength of  $550\ \text{nm}$  (corresponding to the peak wavelength of the employed light source).

Using an MPI grid of  $16 \times 16 \times 16$  on *JUQUEEN*, each simulation run (i. e. the calculation of one configuration, one wavelength, and one angle of incidence) consumed between 7000–8000 CPU hours, required a minimum memory between 260–360 GB, and lasted between 1:45–2:00 hours.

**Computation of the transmitted light intensities.** Supplementary Fig. 10 shows how the 3D-PLI measurement was modeled by means of FDTD simulations.

For the simulations, a mathematically equivalent polarimetric setup of the employed microscope was considered (see Supplementary Fig. 10 on the left) in which the sample is illuminated by (left-handed) circularly polarized light and analyzed by a rotating linear polarizer.

The propagation of the light wave through the sample (fiber configuration) was computed by TDME3D, yielding a superposition of monochromatic plane waves with different wave vectors  $\vec{k}$ :  $\vec{E}_{0,k}(\vec{r}, t) = \vec{E}_{0,k} \cos(\vec{k} \cdot \vec{r} - \omega t + \phi)$ , where  $\vec{r}$  and  $t$  are coordinates in space and time,  $\omega$  is the angular frequency, and  $\phi$  is the phase. Before further processing, the electromagnetic field components were shifted in the  $x, y, z$ -direction to the middle of the corresponding Yee cell, respectively. To study how much light is scattered under a certain angle (wave vector  $\vec{k}$ ), the *scattering pattern* was computed, i. e. the intensity per wave vector normalized by the ingoing light intensity ( $I_0$ ) per image pixel (px):  $I_k = |\vec{E}_{0,k}|^2 / (I_0 / \# \text{px})$ .

To model the 3D-PLI measurement, the resulting electric field vectors were processed through a rotating linear polarizer represented by its Jones matrix [33].

Propagation of the electromagnetic wave between specimen and camera detector was assumed to be free. The objective lens of the microscope was assumed to be ideal and both sample and detector were assumed to lie within the corresponding focal planes of the lens. The numerical aperture ( $\text{NA} \approx 0.15$ ) of the objective lens was modeled by considering only waves with directions of propagation  $\vec{k}$  that fulfill  $\theta_k \leq \arcsin(\text{NA})$ , i. e. only  $k$ -vectors with angles  $\theta_k \leq 8.6^\circ$  were used for processing.

The camera sensor contains an array of spherical microlenses which bundle the light onto subjacent photodiodes for each image pixel. As-

suming perfect microlenses and photodiodes that are completely covered by one microlens, respectively, the microlenses were modeled by applying a moving average over the area of the microlens. Instead of taking the magnification and the physical size of the microlenses into account, the microlenses were modeled with a diameter of  $1.33\ \mu\text{m}$  corresponding to the pixel size of the microscope in object space. To obtain the full image information (independent of the detector pixel position), no rasterizing was applied.

The light intensity recorded by the camera was computed as the absolute squared value of the electric field vector (neglecting angle dependencies due to the small numerical aperture). To compute the intensity at a certain point  $\vec{r}$  in the image plane, the electric field vectors were summed over  $\vec{k}$  and averaged over time. The resulting intensity  $I(\vec{r}, \rho)$  was written in terms of a Fourier series and normalized by the ingoing light intensity per pixel:  $I_N(\vec{r}, \rho) = I(\vec{r}, \rho) / (I_0 / \# \text{px})$ . The Fourier coefficient of order zero  $a_{0,N}$  was used to compute the simulated transmittance images  $I_{T,N}$ .

The computation of the transmitted light intensities is described in Supplementary Note 3 in more detail.

**Error estimation of simulation results.** When modeling the optical components of the imaging system, the limitations of the simulation software need to be taken into account: the simulated light wave is completely polarized and coherent, the materials are characterized by isotropic refractive indices, and size and resolution of the simulated geometries are limited due to finite computing time.

Using completely polarized light for the simulations implies that the optical elements are assumed to be ideal (unpolarized light source, ideal polarizing filters, no polarization-sensitivity of the camera). For the employed polarizing microscope, these assumptions are reasonable because the optical components are of high quality. Moreover, the transmittance can be considered to be mostly independent from the polarization properties of the imaging system.

The LED used for the 3D-PLI measurements emits light with different wavelengths ( $\lambda = 550 \pm 5\ \text{nm}$ ) and angles of incidence ( $\theta_{\max} < 3^\circ$ ). To model this incoherent and diffusive light source, several simulation runs with different wavelengths  $\lambda$  and angles of incidence ( $\varphi, \theta$ ) were performed, and the resulting intensities were added incoherently. A comparison of simulated and experimental data for a well-defined sample (*USAF-1951* resolution target) revealed that the light source can sufficiently be modeled by three different wavelengths ( $\lambda = \{545, 550, 555\}\ \text{nm}$ ) weighted according to the wavelength spectrum, and five angles of incidence ( $\theta = 0^\circ; \theta = 3^\circ, \varphi = \{0^\circ, 90^\circ, 180^\circ, 270^\circ\}$ ). As the transmittance curves for the bundle of densely grown fibers look similar for these wavelengths and angles of incidence (see Supplementary Fig. 18b), the simulations were only performed for a single wavelength ( $\lambda = 550\ \text{nm}$ ) and normally incident light.

To further reduce computing time, the presented simulations were performed for a reduced sample size ( $30 \times 30 \times 30\ \mu\text{m}^3$ ) and 200 time steps. Simulations with larger sample sizes in  $x/y$  and more time steps yield similar results. In addition, the simulations were performed with the largest possible Yee mesh size ( $\Delta = 25\ \text{nm}$ ): smaller mesh sizes yield similar transmittance curves for the bundle of densely grown fibers (see black crosses in Supplementary Fig. 18b).

To estimate the accuracy of the simplified nerve fiber model (axon surrounded by double myelin layers), a single fiber was simulated for different numbers of myelin layers (see Supplementary Note 4 and Fig. 17). The transmittance values for a fiber with double myelin layers ( $\Delta = 25\ \text{nm}$ ) and for a fiber with 43 thin layers ( $\Delta = 3\ \text{nm}$ ) differ by less than 3%. Therefore, the presented simulations were performed for fibers with double myelin layers to enable larger Yee mesh sizes and to reduce computing time.

## REFERENCES

- [1] M. Axer, K. Amunts, D. Grässel, C. Palm, J. Dammers, H. Axer, U. Pietrzyk, and K. Zilles. A novel approach to the hu-

- man connectome: Ultra-high resolution mapping of fiber tracts in the brain. *NeuroImage*, 54(2):1091–1101, 2011. doi: [10.1016/j.neuroimage.2010.08.075](https://doi.org/10.1016/j.neuroimage.2010.08.075).
- [2] M. Axer, D. Gräßel, M. Kleiner, J. Dammers, T. Dickscheid, J. Reckfort, T. Hütz, B. Eiben, U. Pietrzyk, K. Zilles, and K. Amunts. High-resolution fiber tract reconstruction in the human brain by means of three-dimensional polarized light imaging. *Frontiers in Neuroinformatics*, 5(34):1–13, 2011. doi: [10.3389/fninf.2011.00034](https://doi.org/10.3389/fninf.2011.00034).
- [3] M. Menzel, K. Michielsen, H. De Raedt, J. Reckfort, K. Amunts, and M. Axer. A Jones matrix formalism for simulating three-dimensional polarized light imaging of brain tissue. *Journal of the Royal Society Interface*, 12:20150734, 2015. doi: [10.1098/rsif.2015.0734](https://doi.org/10.1098/rsif.2015.0734).
- [4] M. Dohmen, M. Menzel, H. Wiese, J. Reckfort, F. Hanke, U. Pietrzyk, K. Zilles, K. Amunts, and M. Axer. Understanding fiber mixture by simulation in 3D Polarized Light Imaging. *NeuroImage*, 111:464–475, 2015. ISSN 1053-8119. doi: [10.1016/j.neuroimage.2015.02.020](https://doi.org/10.1016/j.neuroimage.2015.02.020).
- [5] M. Menzel, J. Reckfort, D. Weigand, H. Köse, K. Amunts, and M. Axer. Diattenuation of brain tissue and its impact on 3D polarized light imaging. *Biomedical Optics Express*, 8(7):3163–3197, 2017. doi: [10.1364/BOE.8.003163](https://doi.org/10.1364/BOE.8.003163).
- [6] H.-J. Schwarzmaier, A. Yaroslavsky, I. Yaroslavsky, T. Goldbach, T. Kahn, F. Ulrich, P. C. Schulze, and R. Schober. Optical properties of native and coagulated human brain structures. *SPIE*, 2970:492–499, 1997. doi: [10.1117/12.275082](https://doi.org/10.1117/12.275082).
- [7] A. N. Yaroslavsky, P. C. Schulze, I. V. Yaroslavsky, R. Schober, F. Ulrich, and H.-J. Schwarzmaier. Optical properties of selected native and coagulated human brain tissues in vitro in the visible and near infrared spectral range. *Physics in Medicine and Biology*, 47:2059–2073, 2002. URL <http://stacks.iop.org/PMB/47/2059>.
- [8] K. Zilles. *The Cortex of the Rat – A Stereotaxic Atlas*. Springer, Berlin Heidelberg, 1985. doi: [10.1007/978-3-642-70573-1](https://doi.org/10.1007/978-3-642-70573-1).
- [9] G. Paxinos and C. Watson. *The Rat Brain in Stereotaxic Coordinates*. Academic Press, 6 edition, 2007.
- [10] E. A. Papp, T. B. Leergard, E. Calabrese, G. A. Johnson, and J. G. Bjaalie. Waxholm Space atlas of the Sprague Dawley rat brain. *NeuroImage*, 97:374–386, 2014. doi: [10.1016/j.neuroimage.2014.04.001](https://doi.org/10.1016/j.neuroimage.2014.04.001).
- [11] R. P. Woods, S. C. Fears, M. J. Jorgensen, L. A. Fairbanks, A. W. Toga, and N. B. Freimer. A web-based brain atlas of the vervet monkey, chlorocebus aethiops. *NeuroImage*, 54(3):1872–1880, 2011. doi: [10.1016/j.neuroimage.2010.09.070](https://doi.org/10.1016/j.neuroimage.2010.09.070).
- [12] <http://www.loni.usc.edu/Research/Atlases/Data/vervet/vervetatlas/vervetatlas.html>. University of Southern California, Laboratory of Neuro Imaging, January 2018.
- [13] K. Zilles, N. Palomero-Gallagher, D. Gräßel, P. Schlömer, M. Cremer, R. Woods, K. Amunts, and M. Axer. High-resolution fiber and fiber tract imaging using polarized light microscopy in the human, monkey, rat, and mouse brain. In Kathleen S. Rockland, editor, *Axons and Brain Architecture*, chapter 18, pages 369–389. Elsevier Academic Press, San Diego, 2015.
- [14] J. Reckfort. *New Approaches to the Interpretation of 3D-Polarized Light Imaging Signals for an Advanced Extraction of Fiber Orientation*. PhD thesis, University of Wuppertal, 2015.
- [15] J. Reckfort, H. Wiese, U. Pietrzyk, K. Zilles, K. Amunts, and M. Axer. A multiscale approach for the reconstruction of the fiber architecture of the human brain based on 3D-PLI. *Frontiers in Neuroanatomy*, 9(118):1–11, 2015. doi: [10.3389/fnana.2015.00118](https://doi.org/10.3389/fnana.2015.00118).
- [16] M. Zeineh, N. Palomero-Gallagher, M. Axer, D. Gräßel, M. Goubran, A. Wree, R. Woods, K. Amunts, and K. Zilles. Direct visualization and mapping of the spatial course of fiber tracts at microscopic resolution in the human hippocampus. *Cerebral Cortex*, 2016. doi: [10.1093/cercor/bhw010](https://doi.org/10.1093/cercor/bhw010).
- [17] S. Klein, M. Staring, K. Murphy, M. A. Viergever, and J. P. W. Pluim. elastix: A toolbox for intensity-based medical image registration. *IEEE Transactions on Medical Imaging*, 29(1):196–205, 2010. doi: [10.1109/TMI.2009.2035616](https://doi.org/10.1109/TMI.2009.2035616).
- [18] D. P. Shamonin, E. E. Bron, B. P. F. Lelieveldt, M. Smits, S. Klein, and M. Staring. Fast parallel image registration on CPU and GPU for diagnostic classification of Alzheimer’s disease. *Frontiers in Neuroinformatics*, 7:50, 2013. doi: [10.3389/fninf.2013.00050](https://doi.org/10.3389/fninf.2013.00050).
- [19] B. B. Avants, C. L. Epstein, M. Grossman, and J. C. Gee. Symmetric diffeomorphic image registration with cross-correlation: Evaluating automated labeling of elderly and neurodegenerative brain. *Medical Image Analysis*, 12(1):26–41, 2008. doi: [10.1016/j.media.2007.06.004](https://doi.org/10.1016/j.media.2007.06.004).
- [20] B. B. Avants, N. J. Tustison, G. Song, P. A. Cook, A. Klein, and J. C. Gee. A reproducible evaluation of ANTs similarity metric performance in brain image registration. *NeuroImage*, 54(3):2033–2044, 2011. doi: [10.1016/j.neuroimage.2010.09.025](https://doi.org/10.1016/j.neuroimage.2010.09.025).
- [21] National library of medicine insight segmentation and registration toolkit (ITK), <https://itk.org/>.
- [22] D. Wagner and D. Schmalstieg. ARToolKitPlus for pose tracking on mobile devices. In *Proceedings of the 12th Computer Vision Winter Workshop*, pages 139–146, 2007.
- [23] M. Schober, P. Schlömer, M. Cremer, H. Mohlberg, A.-M. Huynh, N. Schubert, M.E. Kirlangic, K. Amunts, and M. Axer. Reference volume generation for subsequent 3D reconstruction of histological sections. In *Proc. of Bildverarbeitung für die Medizin (BVM), Lübeck, Germany*, pages 143–148, 2015.
- [24] L. Silvestri, A. L. Allegra Mascaro, I. Costantini, L. Sacconi, and F. S. Pavone. Correlative two-photon and light sheet microscopy. *Methods*, 66(2):268–272, 2014. doi: [10.1016/j.jymeth.2013.06.013](https://doi.org/10.1016/j.jymeth.2013.06.013).
- [25] I. Costantini, M. Menzel, L. Silvestri, N. Schubert, M. Axer, K. Amunts, and F. S. Pavone. Polarized Light Imaging and Two-Photon Fluorescence Microscopy correlative approach for 3D reconstruction of the orientation of myelinated fibers. *Optics in the Life Sciences Congress, OSA Technical Digest (online), paper BrW4B.5*, 2017. doi: [10.1364/BRAIN.2017.BrW4B.5](https://doi.org/10.1364/BRAIN.2017.BrW4B.5).
- [26] A. Taflove and S. C. Hagness. *Computational Electrodynamics: The Finite-Difference Time-Domain Method*. Artech House, MA USA, 3 edition, 2005. ISBN 1580538320.
- [27] K. S. Yee. Numerical solution of initial boundary value problems involving Maxwell’s equations in isotropic media. *IEEE Transactions on Antennas and Propagation*, 14:302–307, 1966. doi: [10.1109/TAP.1966.1138693](https://doi.org/10.1109/TAP.1966.1138693).

- [28] M. Menzel, M. Axer, H. De Raedt, and K. Michielsen. Finite-Difference Time-Domain Simulation for Three-Dimensional Polarized Light Imaging. In K. Amunts, L. Grandinetti, T. Lippert, and N. Petkov, editors, *Brain-Inspired Computing. Brain-Comp 2015. Lecture Notes in Computer Science*, volume 10087, chapter 6, pages 73–85. Springer International Publishing, Cham, 2016. doi: [10.1007/978-3-319-50862-7\\_6](https://doi.org/10.1007/978-3-319-50862-7_6).
- [29] K. Michielsen, H. de Raedt, and D. G. Stavenga. Reflectivity of the gyroid biophotonic crystals in the ventral wing scales of the Green Hairstreak butterfly, *Callophrys rubi*. *Journal of the Royal Society Interface*, 7:765–771, 2010. doi: [10.1098/rsif.2009.0352](https://doi.org/10.1098/rsif.2009.0352).
- [30] B. D. Wilts, K. Michielsen, H. De Raedt, and D. G. Stavenga. Sparkling feather reflections of a bird-of-paradise explained by finite-difference time-domain modeling. *Proceedings of the National Academy of Sciences*, 2014. doi: [10.1073/pnas.1323611111](https://doi.org/10.1073/pnas.1323611111).
- [31] H. De Raedt. Advances in unconditionally stable techniques. In A. Taflov and S. C. Hagness, editors, *Computational Electrodynamics: The Finite-Difference Time-Domain Method*, chapter 18. Artech House, MA USA, 3 edition, 2005. ISBN 1580538320.
- [32] Jülich Supercomputing Centre. JUQUEEN: IBM Blue Gene/Q Supercomputer System at the Jülich Supercomputing Centre. *Journal of large-scale research facilities*, 1, A1, 2015. doi: [10.17815/jlsrf-1-18](https://doi.org/10.17815/jlsrf-1-18).
- [33] R. C. Jones. A new calculus for the treatment of optical systems. *Journal of the Optical Society of America*, 31:488–503, 1941. doi: [10.1364/JOSA.31.000488](https://doi.org/10.1364/JOSA.31.000488).
- [34] Jülich Supercomputing Centre. JURECA: General-purpose supercomputer at Jülich Supercomputing Centre. *Journal of large-scale research facilities*, 2(A62), 2016. doi: [10.17815/jlsrf-2-121](https://doi.org/10.17815/jlsrf-2-121). URL <http://dx.doi.org/10.17815/jlsrf-2-121>.
- [35] H. Altendorf and D. Jeulin. Random walk based stochastic modeling of 3D fiber systems. *Physical Review E : Statistical, Non-linear, and Soft Matter Physics, American Physical Society*, 83 (4), 2010. doi: [10.1103/PhysRevE.83.041804](https://doi.org/10.1103/PhysRevE.83.041804).
- [36] L. Chapelle, M. Lévesque, P. Brøndsted, M. R. Foldschack, and Y. Kusano. Generation of non-overlapping fiber architecture. In *Proceedings of the 20th International Conference on Composite Materials ICCM20 Secretariat*, 2015.
- [37] R. H. Quarles, W. B. Macklin, and P. Morell. Myelin formation, structure and biochemistry. In G. Siegel, R. W. Albers, S. Brady, and D. Price, editors, *Basic Neurochemistry: Molecular, Cellular and Medical Aspects*, pages 51–71. Elsevier Academic Press, Burlington, MA, 7 edition, 2006. ISBN 0-12-088397-X.
- [38] C. Hildebrand, S. Remahl, H. Persson, and C. Bjartmar. Myelinated nerve fibers in the CNS. *Progress in Neurobiology*, 40: 319–384, 1993.
- [39] R. E. Martenson. *Myelin: Biology and Chemistry*. CRC Press, USA, 1992. ISBN 0-8493-8849-X.
- [40] D. W. Lee, X. Banquy, K. Kristiansen, Y. Kaufman, J. M. Boggs, and J. N. Israelachvili. Lipid domains control myelin basic protein adsorption and membrane interactions between model myelin lipid bilayers. *PNAS*, pages E768–E775, 2014. doi: [10.1073/pnas.1401165111](https://doi.org/10.1073/pnas.1401165111).
- [41] H.-J. van Manen, P. Verkuijlen, P. Wittendorp, V. Subramaniam, T. K. van den Berg, D. Roos, and C. Otto. Refractive index sensing of green fluorescent proteins in living cells using fluorescence lifetime imaging microscopy. *Biophysical Letters*, 94(8):L67–69, 2008. doi: [10.1529/biophysj.107.127837](https://doi.org/10.1529/biophysj.107.127837).
- [42] F. A. Duck. *Physical Properties of Tissue: A Comprehensive Reference Book*. Academic Press, San Diego, 1990. ISBN 9780122228001.
- [43] P. Morell, R. H. Quarles, and W. T. Norton. Formation, structure, and biochemistry of myelin. In G. J. Siegel, editor, *Basic Neurochemistry - Molecular, Cellular, and Medical Aspects*, pages 109–136. Raven Press, New York, 4 edition, 1989. ISBN 0881673439.
- [44] Jingjing Sun, Sung Jin Lee, Lei Wu, Malisa Sarntinoranont, and Huikai Xie. Refractive index measurement of acute rat brain tissue slices using optical coherence tomography. *Optics Express*, 20(2):1084–1095, 2012. doi: [10.1364/OE.20.001084](https://doi.org/10.1364/OE.20.001084).
- [45] E. Collett. *Field Guide to Polarization*. SPIE – The International Society for Optical Engineering, Washington, 2005. ISBN 0-8194-5868-6.
- [46] T. E. Oliphant. Python for scientific computing. *Computing in Science & Engineering*, 9:10–20, 2007. doi: [10.1109/MCSE.2007.58](https://doi.org/10.1109/MCSE.2007.58).
- [47] S. van der Walt, S. C. Colbert, and G. Varoquaux. The NumPy array: A structure for efficient numerical computation. *Computing in Science & Engineering*, 13:22–30, 2011. doi: [10.1109/MCSE.2011.37](https://doi.org/10.1109/MCSE.2011.37).
- [48] J. W. Cooley and J. W. Tukey. An algorithm for the machine calculation of complex Fourier series. *Mathematics of Computation*, 19(90):297–301, 1965.

## ACKNOWLEDGMENTS

This project has received funding from the Helmholtz Association portfolio theme *Supercomputing and Modeling for the Human Brain*, from the European Union’s Horizon 2020 Research and Innovation Programme under Grant Agreement No. 720270 (*Human Brain Project SGA1*), and from the National Institutes of Health under grant agreement No. R01MH 092311. We gratefully acknowledge the computing time granted by the JARA-HPC Vergabegremium and VSR commission on the supercomputer *JURECA* [34] and the JARA-HPC Partition part of the supercomputer *JUQUEEN* [32] at Forschungszentrum Jülich GmbH. We thank Markus Cremer, Christian Schramm, and Patrick Nysten for the preparation of the histological brain sections, David Gräbel and Isabelle Mafoppa Fomat for the 3D-PLI measurements, Philipp Schlömer for generating the transmittance and retardation images, Martin Schober, Marcel Huysegoms, and Sascha Münzing for image registration, Felix Matuschke for developing the algorithms to generate the fiber configurations, Irene Costantini, Ludovico Silvestri, and Francesco S. Pavone for the TPFM measurements, and Sebastian Bludau for the transmission microscopy measurement.

## AUTHOR CONTRIBUTIONS

M.M. substantially contributed to the conception and design of the study as well as to the analysis and interpretation of the experimental and simulated data and to the theoretical considerations. She analyzed the measurements, carried out the simulations, created the figures, and wrote the manuscript. M.A. participated in the conception and design of the study, contributed to the analysis and interpretation of the data, and to the revision of the manuscript. H.D.R. contributed to the interpretation of the simulated data, to the theoretical considerations, and to the revision of the manuscript. I.C., L.S., and F.S.P. produced the TPFM measurements. K.A. contributed to the anatomical content of the study. K.M. participated in the design of the study, contributed to the interpretation of the simulated data, to the theoretical considerations, and to the revision of the manuscript. All authors read the final manuscript and gave approval for publication.

## SUPPLEMENTARY INFORMATION

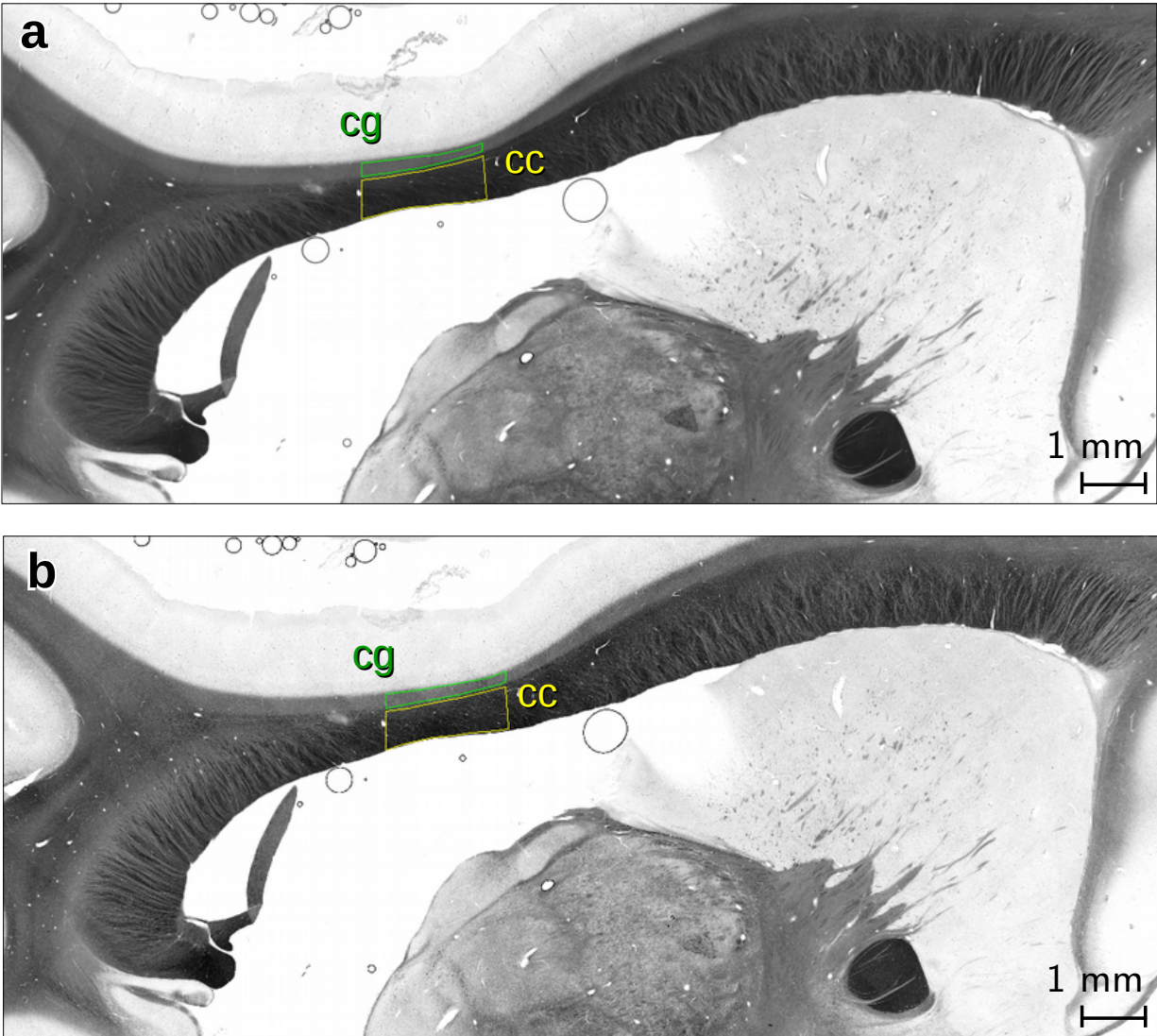


**Fig. 7. Supplementary Figure | Polarized light imaging vs. standard transmission microscopy.** Detail of a sagittal vervet brain section (neighbored section to the one shown in Fig. 1b): **a** Normalized transmittance image obtained from 3D-PLI measurement (LED wavelength:  $550 \pm 5$  nm, objective lens: 5 $\times$  Plan Fluor, numerical aperture: 0.15, resolution:  $1.33 \mu\text{m}/\text{px}$ , see [Methods](#)). **b** Transmission microscopy image obtained from ZEISS Axio Imager Vario with unpolarized light (microLED wavelength: 400–700 nm, objective lens: 5 $\times$  Plan Apochromat, numerical aperture: 0.16, resolution:  $0.91 \mu\text{m}/\text{px}$ ). The corpus callosum (cc) contains mainly out-of-plane fibers, while the cingulum (cg) contains mainly in-plane fibers (cf. Fig. 1). The mean transmitted light intensity of the selected region in the corpus callosum is about 53% (a) and 32% (b) less than the mean transmitted light intensity of the selected region in the cingulum, respectively. This demonstrates that the same effects (less transmitted light intensity in regions with out-of-plane fiber structures than in regions with in-plane fiber structures) can also be observed in standard transmission microscopy which uses unpolarized light.

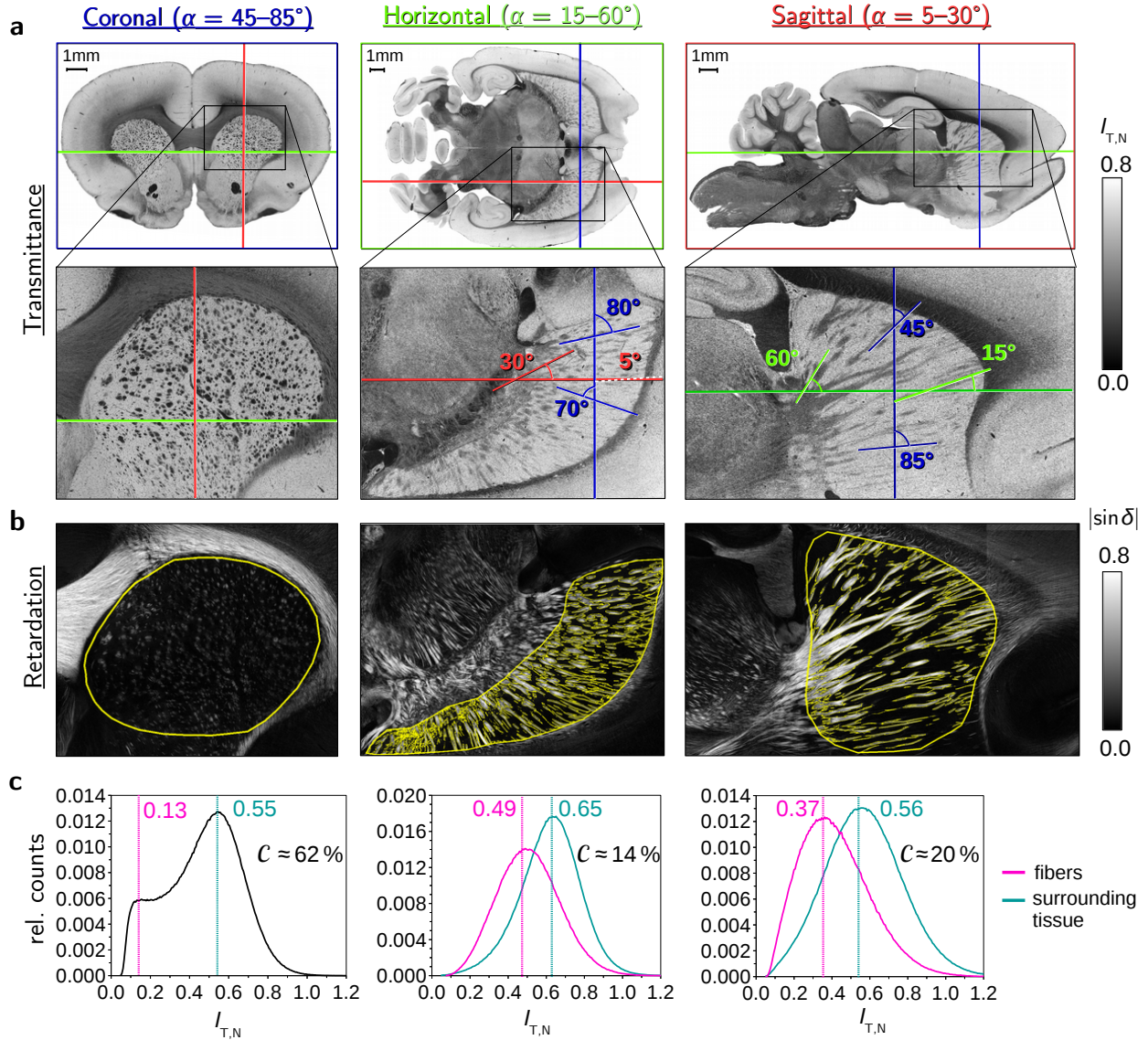


**Fig. 8. Supplementary Figure | Transmittance contrast of cortical striatum fibers in coronal, horizontal, and sagittal rat brain sections.**

**a** Normalized transmittance images ( $I_{T,N}$ ) of a coronal, horizontal, and sagittal rat brain section obtained from 3D-PLI measurements with  $1.33 \mu\text{m}$  pixel size (see [Methods](#)). The colored lines indicate the approximate position of the section planes. The enlarged views show the region of the caudate putamen and the maximum and minimum angles under which the striatum fibers are oriented with respect to the section planes. **b** Corresponding retardation images ( $|\sin \delta|$ ) of the enlarged views. The image contrast was used to select regions with fibers and with surrounding tissue in the caudate putamen (yellow). **c** Histograms of the transmittance values ( $I_{T,N}$ ) for the selected fiber regions (pink) and the surrounding tissue (cyan) in the caudate putamen. For the coronal brain section, the retardation image cannot be used to separate the fibers from the surrounding tissue because the fibers are oriented almost perpendicularly to the image plane which leads to a small retardation signal and a small image contrast. Therefore, the histogram was computed over the whole selected region and the peak with lower (larger) transmittance was assumed to belong to fibers (surrounding tissue). The contrast values were computed from the respective peak values (numbers in pink and cyan) via:  $C = (\max - \min) / (\max + \min)$ . The contrast for steep fibers is much larger ( $\alpha = 45\text{--}85^\circ$ :  $C \approx 62\%$ ) than for flat fibers ( $\alpha = 5\text{--}60^\circ$ :  $C \approx 14\text{--}20\%$ ).

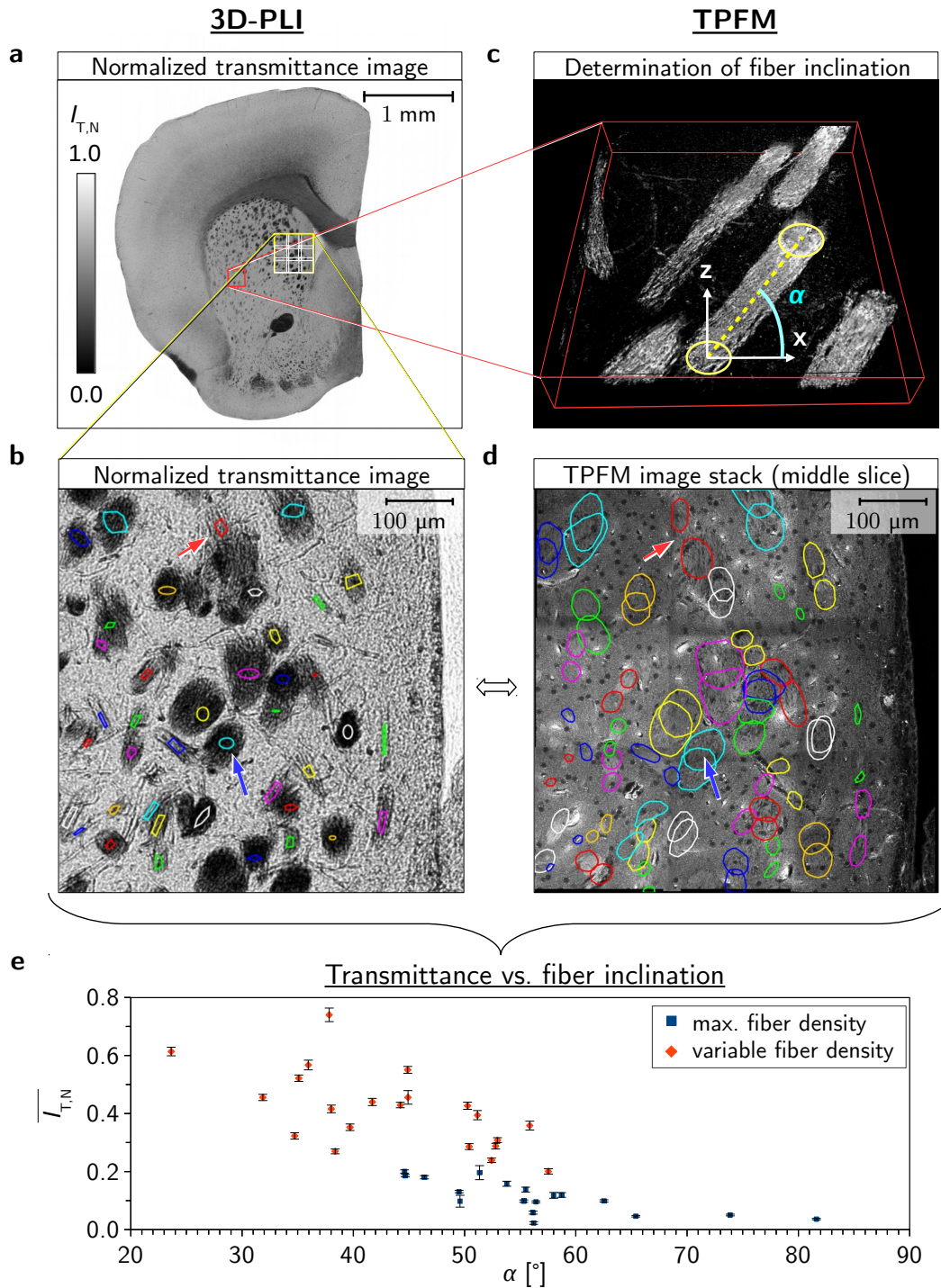


**Fig. 9. Supplementary Figure | Transmittance vs. fiber inclination.** A coronal, 60  $\mu\text{m}$  thin section from the left hemisphere of a mouse brain was measured with 3D-PLI (voxel size:  $1.33 \times 1.33 \times 60 \mu\text{m}^3$ ) and with TPFM (voxel size:  $0.24 \times 0.24 \times 1 \mu\text{m}^3$ ), see [Methods](#). The TPFM measurements were performed for a region of  $3 \times 3$  tiles in the caudate putamen: **a** normalized transmittance image of the coronal mouse brain section, **b** normalized transmittance image of the selected region in the caudate putamen, **c** single tile of a contrast-enhanced TPFM image stack demonstrating the determination of the fiber inclination angle  $\alpha$ , **d** middle slice of the TPFM image stack for the selected region in the caudate putamen, **e** mean normalized transmittance values  $\overline{I_{T,N}}$  plotted against the determined fiber inclination angles  $\alpha$ . The inclination angles of 40 fiber bundles were determined from the mid point positions of the cross-sections in the first and the last slice of the TPFM image stack (see colored shapes in Fig. d), the transmittance values were evaluated in the middle of the corresponding fiber bundles (see colored shapes in Fig. b). The blue (red) data points in the scatter plot belong to regions that are (are not) completely filled with nerve fibers, cf. blue (red) arrows in Figs. b,d. The error bars indicate the standard error of the mean for the evaluated transmittance values. Although the values are broadly distributed, the scatter plot shows a clear tendency towards a decrease in transmittance with increasing fiber inclination, also in regions with maximum fiber density.

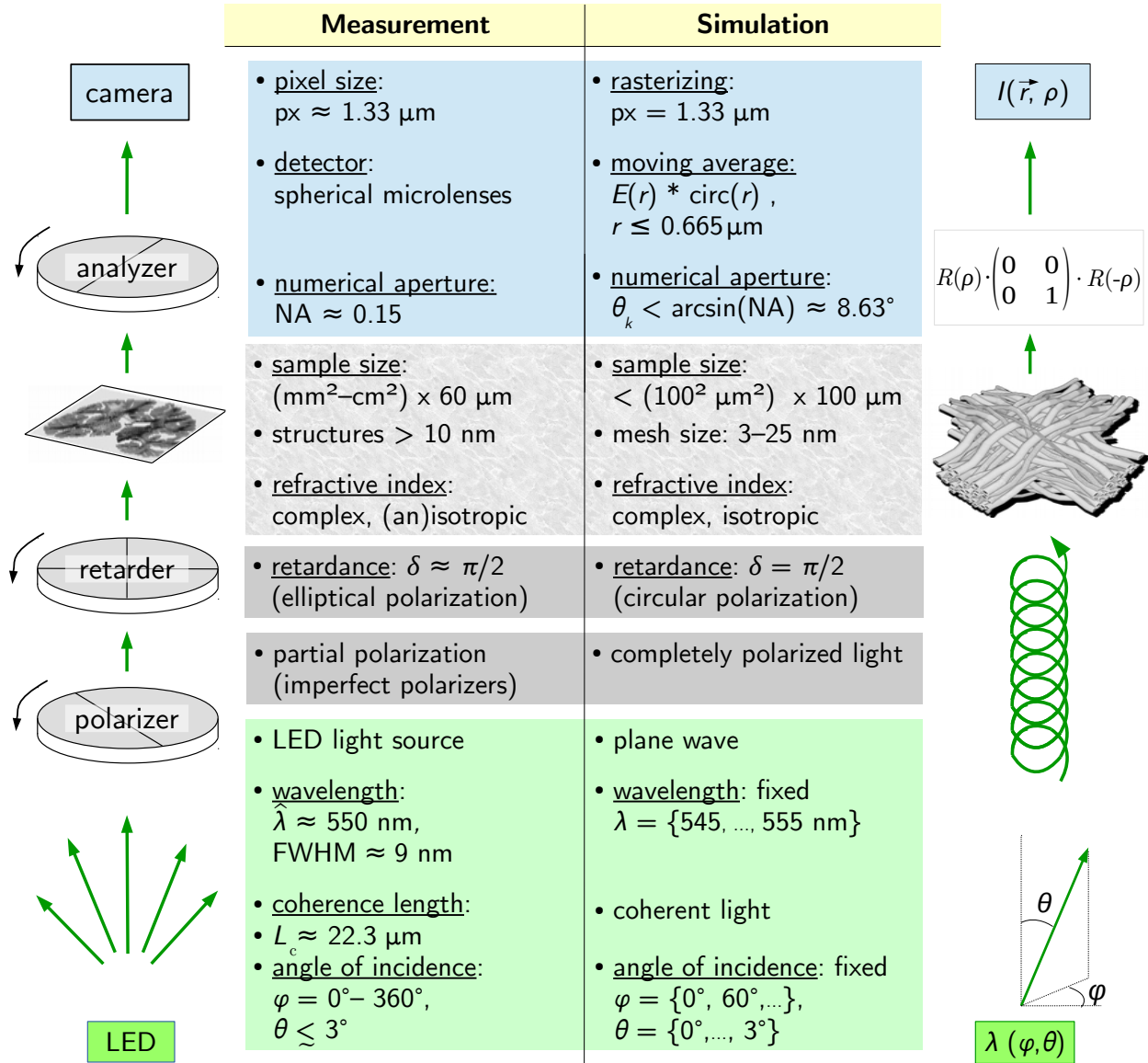


**Fig. 10. Supplementary Figure | Modeling the 3D-PLI measurement.** On the left-hand side, the optical components of the polarimeter are characterized (the order of the polarizing filters is different than in the measurement, but the setup is mathematically equivalent): light source (green), polarizer/retarder (dark gray), sample (light gray), objective lens/detector (blue). The table and figure on the right-hand side show how the optical elements were modeled by FDTD simulations: The incoherent and diffusive light source (LED) with peak wavelength  $\hat{\lambda}$  and full-width at half-maximum (FWHM) was modeled by performing several simulation runs with plane waves that have different wavelengths ( $\lambda$ ) and angles of incidence ( $\varphi, \theta$ ). The modeled light source emits coherent light that is circularly polarized. The tissue sample was represented by an artificial fiber architecture, the rotating analyzer by a rotated Jones matrix [33] (with rotation matrix  $R(\rho)$ ). The numerical aperture (NA) of the imaging system was modeled by considering only wave vector angles  $\theta_k < \arcsin(\text{NA})$ . The spherical microlenses of the camera detector were modeled by performing a moving average over the area of the microlens with radius  $1.33 \mu\text{m}/2$ .

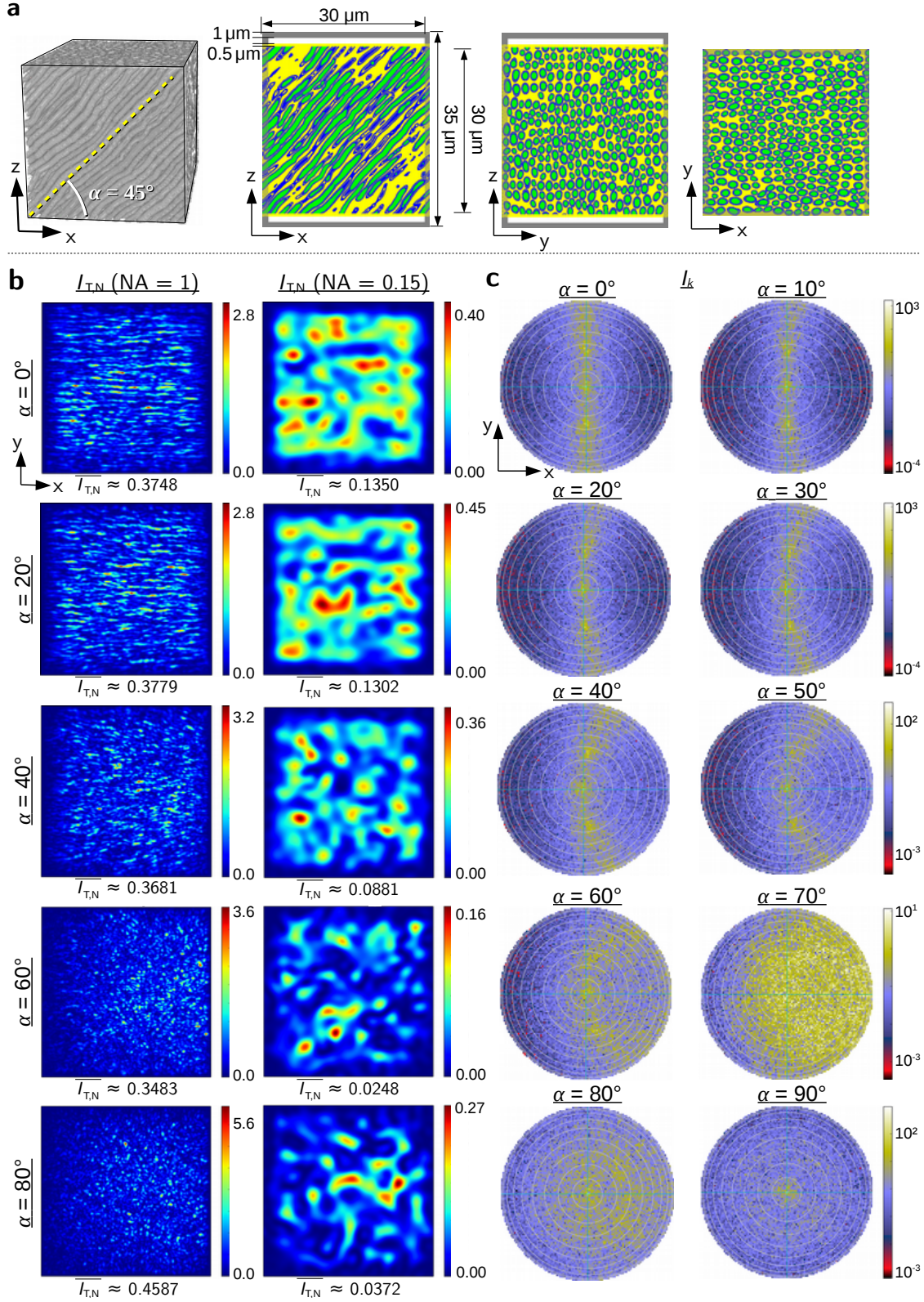


**Fig. 11. Supplementary Figure | Simulated transmittance and light-scattering patterns for different fiber inclinations.** **a** 3D-view and cross-sections through mid-planes of the simulation volume for the bundle of densely grown fibers with inclination  $\alpha = 45^\circ$ . **b-c** Transmittance images ( $I_{T,N}$ ) and light-scattering patterns ( $I_k$ ) computed from a simulated 3D-PLI measurement (see [Methods](#)) for different fiber inclination angles  $\alpha$  (using a normally incident plane wave with 550 nm wavelength and simulation parameters specified in Supplementary Tab. 2). The transmittance images were computed for the numerical aperture of the imaging system (NA = 0.15) and for NA = 1. Note that the value ranges differ between images. With increasing fiber inclination, the scattering increases which leads to a decrease in the mean transmittance values  $\overline{I_{T,N}}$  for NA = 0.15.

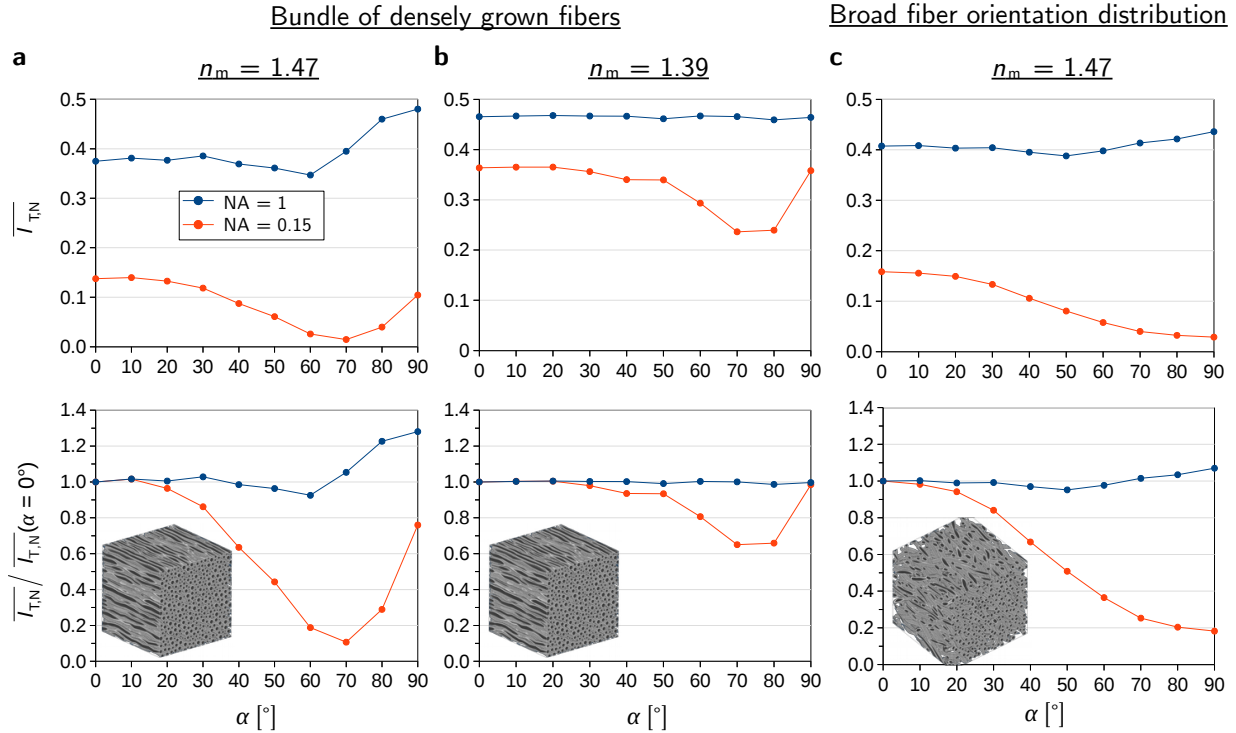


**Fig. 12. Supplementary Figure | Simulated transmittance curves.** Mean normalized transmittance values  $\overline{I_{T,N}}$  plotted against the inclination angles  $\alpha$  for different fiber bundles and different myelin refractive indices  $n_m$  (see Supplementary Note 1 and 2): **a** bundle of densely grown fibers with  $n_m = 1.47$  (corresponds to given literature values of lipids), **b** bundle of densely grown fibers with  $n_m = 1.39$  (the reduced myelin refractive index models tissue with long embedding time), **c** bundle with broad fiber orientation distribution and  $n_m = 1.47$ . The red curves were computed from 3D-PLI simulations for the numerical aperture of the imaging system (NA = 0.15) and the blue curves for NA = 1. To enable a better comparison between horizontal and vertical fibers, the lower figures show the transmittance curves normalized by the mean transmittance of the horizontal fiber bundle, respectively. The 3D-PLI simulations were performed as described in Methods (using a normally incident plane wave with 550 nm wavelength and simulation parameters specified in Supplementary Tab. 2). A reduced myelin refractive index (long embedding time) leads to larger transmittance values and a smaller decrease for steep fibers for NA = 0.15. While the transmittance curves for the bundle of densely grown fibers show a minimum for steep fibers ( $\alpha = 70\text{--}80^\circ$ ), the mean transmittance values for the bundle with broad fiber orientation distribution decrease monotonically with increasing fiber inclination.

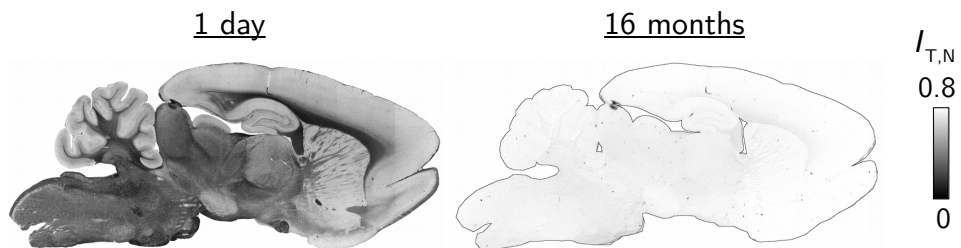


**Fig. 13. Supplementary Figure | Transmittance vs. tissue aging.** Normalized transmittance image  $I_{T,N}$  of the sagittal rat brain section (Fig. 1a) one day after tissue embedding (see Methods) and 16 months later. With increasing time after tissue embedding, the brain section becomes more transparent.

## Supplementary Note 1. Generation of artificial fiber configurations

### *Generation of the densely grown fiber bundle*

The bundle of densely grown fibers (see Fig. 3a) was generated by in-house developed software:  $N = 700$  circles with uniformly distributed diameters ( $d \in [1.0, 1.6] \mu\text{m}$ ) were randomly uniformly placed in the xy-plane (in an area of  $45 \times 30 \mu\text{m}^2$ ). The circles were initialized with a random speed (max.  $0.1 \mu\text{m}$  displacement per step) and collided with each other (assuming elastic collision with particle mass  $r^2$ ) until a solution was reached without collision in the xy-plane. To obtain well-distributed fibers, the previous step was repeated 250 times before the positions of the circles were stored. To obtain a 3D fiber volume, the circle positions were stored while incrementing the z-position by  $1 \mu\text{m}$  per step. To generate fiber bundles with different inclination angles, the resulting bundle of densely grown fibers was rotated around the y-axis with respect to the center position and cropped to a volume of  $30 \times 30 \times 30 \mu\text{m}^3$ . To prevent fibers from touching each other after discretization, all fiber diameters were reduced by 5%. In the resulting fiber bundle, about 60% of the volume is filled with fibers.

### *Generation of more inhomogeneous fiber bundles*

More inhomogeneous fiber bundles, like the bundle with broad fiber orientation distribution or crossing fibers, were generated by in-house developed software similar to [35, 36], which allows collision control in 3D. Starting from well-distributed straight fibers with  $N = 700$  and  $d \in [1.0, 1.6] \mu\text{m}$  (obtained after 250 steps as described in the previous paragraph), the fibers were divided iteratively into segments of  $2\text{--}5 \mu\text{m}$  and assigned a random displacement in the x-, y-, and z-direction. The resulting fiber segments were split or merged until the length of each segment was again between  $2\text{--}5 \mu\text{m}$ , ensuring that the maximum angle between adjacent segments was less than  $20^\circ$ . When a collision between two segments was detected, the segments were exposed to a small repelling force and the previous step was repeated until no more collisions were detected. To prevent fibers from touching each other, all fiber diameters were reduced by 5%. The resulting fiber bundle was cropped to a volume of  $30 \times 30 \times 30 \mu\text{m}^3$ . The fiber bundles were generated from different configurations of straight fibers and different random displacements:

- *Bundle with broad fiber orientation distribution* (Fig. 3c(ii)): The fiber bundle was generated from a bundle of straight horizontal fibers in the x-direction and a maximum random displacement of  $10 \mu\text{m}$ . In the resulting fiber bundle, about 33% of the volume is filled with fibers. To generate fiber bundles with different inclination angles, the resulting bundle was rotated around the y-axis with respect to the center position.
- *Separate crossing fiber bundles* (Fig. 4a): The bundle of straight horizontal fibers in the x-direction was divided in an upper and a lower bundle of thickness  $z/2$ , respectively. The upper bundle was rotated around the z-axis about the center position by an angle  $+\chi/2$ , the lower bundle was rotated by an angle  $-\chi/2$ , resulting in two separate bundles with crossing angle  $\chi$  (cf. Supplementary Fig. 14a). The resulting fibers were used as input for the algorithm with a maximum displacement of  $1 \mu\text{m}$ . Depending on the crossing angle of the resulting fiber bundle, between 40–50% of the volume is filled with fibers.
- *Interwoven crossing fiber bundles* (Fig. 4a): Each fiber layer in the z-direction of the straight horizontal fiber bundle (oriented in the x-direction) was rotated alternately by  $\pm\chi/2$  (cf. Supplementary Fig. 14b). The resulting fibers were used as input for the algorithm with a maximum displacement of  $1 \mu\text{m}$ . Depending on the crossing angle of the resulting fiber bundles, between 40–50% of the volume is filled with fibers.
- *Mutually orthogonal, interwoven fiber bundles* (Fig. 4b): The straight horizontal fiber bundle (oriented in the x-direction) was divided in three types of alternating layers: one layer was rotated  $+45^\circ$  around the z-axis, one  $-45^\circ$  around the z-axis, and one  $+90^\circ$  around the y-axis, yielding two horizontal fiber bundles in the xy-plane and one vertical fiber bundle oriented along the z-axis. The resulting fibers were used as input for the algorithm with a maximum displacement of  $1 \mu\text{m}$ . In the resulting fiber bundle, about 32% of the volume is filled with fibers.

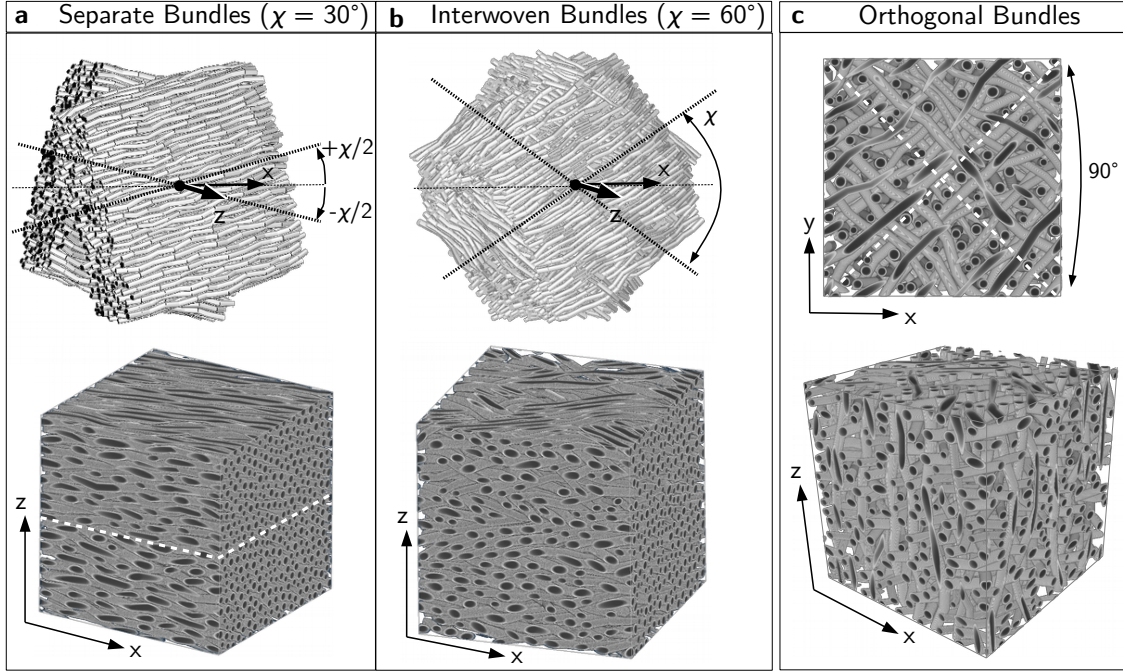


**Fig. 14. Supplementary Figure | Generation of crossing fibers.** **a-b** Separate and interwoven fiber bundles with crossing angle  $\chi$ : The upper figures show the generated bundles before cropping. The lower figures show the bundles after being cropped to a volume of  $30 \times 30 \times 30 \mu\text{m}^3$ . The white dotted line indicates the border between the upper and the lower bundle of the separate crossing fibers. **c** Three mutually orthogonal, interwoven fiber bundles cropped to a volume of  $30 \times 30 \times 30 \mu\text{m}^3$ . The white dotted lines indicate the main directions of the two horizontal fiber bundles in the  $xy$ -plane, the third fiber bundle is oriented in the  $z$ -direction. All fiber configurations were generated from 700 fibers with diameters between 1.0 and 1.6  $\mu\text{m}$ .

### Supplementary Note 2. Model of the nerve fibers

The myelin sheath surrounds most of the axons in the white matter and consists of densely packed cell membranes [37, 38]. Supplementary Fig. 15c shows the layered structure of the myelin sheath: it consists of alternating layers of cell membranes (lipid bilayers of about 5 nm thickness) and intracellular/cytoplasmic or extracellular space (of about 3 nm thickness) [39, 40]. As the extracellular membranes are not fused and swell in water [37, 39], it is assumed that the extracellular space is filled with the glycerin solution used for embedding the brain sections (see Methods).

The refractive indices  $n$  of the layers were estimated from literature values of lipids/membranes ( $n = 1.47$  [41], neglecting any proteins), cytoplasm ( $n = 1.35$  [42]), and glycerin solution ( $n = 1.37$ , measured with digital refractometer).

A simplified model was used to represent the myelin sheath (see Supplementary Fig. 15d): Each cell layer (two lipid bilayers with separating cytoplasm) was considered as one *myelin layer* with an effective refractive index  $n_m = 1.47$  (blue), the extracellular space was considered to be filled with glycerin solution (*glycerin layer*) with a refractive index  $n_g = 1.37$  (yellow). Assuming that the extracellular space increases when being embedded in glycerin, the myelin and glycerin layers were assumed to contribute 3/4 and 1/4 to the overall myelin sheath thickness  $t_{\text{sheath}}$ , respectively. The refractive index of the cytoplasmic layer was neglected in this model.

The myelin sheath thickness contributes approximately one third to the overall fiber radius  $r$  [43]. Hence, the myelin sheath thickness was chosen to be  $t_{\text{sheath}} = 0.35 r$  and the radius of the inner axon  $r_{\text{ax}} = 0.65 r$ . The refractive index of the axon (green) was chosen to correspond to the refractive index of cytoplasm ( $n_{\text{ax}} = 1.35$ ). The myelin sheath was modeled as double myelin layers with thickness  $t_m = 3/7 t_{\text{sheath}}$  each and a single glycerin layer with thickness  $t_g = 1/7 t_{\text{sheath}}$  separating the myelin layers. The nodes of Ranvier and the small space between axon and myelin sheath, the so-called periaxonal space [38], were neglected in this model.

For the FDTD simulations, all fibers were simulated with double myelin layers and with the refractive indices given above. The surrounding medium was assumed to be homogeneous with a refractive index  $n_{\text{surr}} = n_g = 1.37$  (yellow), which corresponds to the refractive index of gray matter [44] as well as to the refractive index of the surrounding glycerin solution.

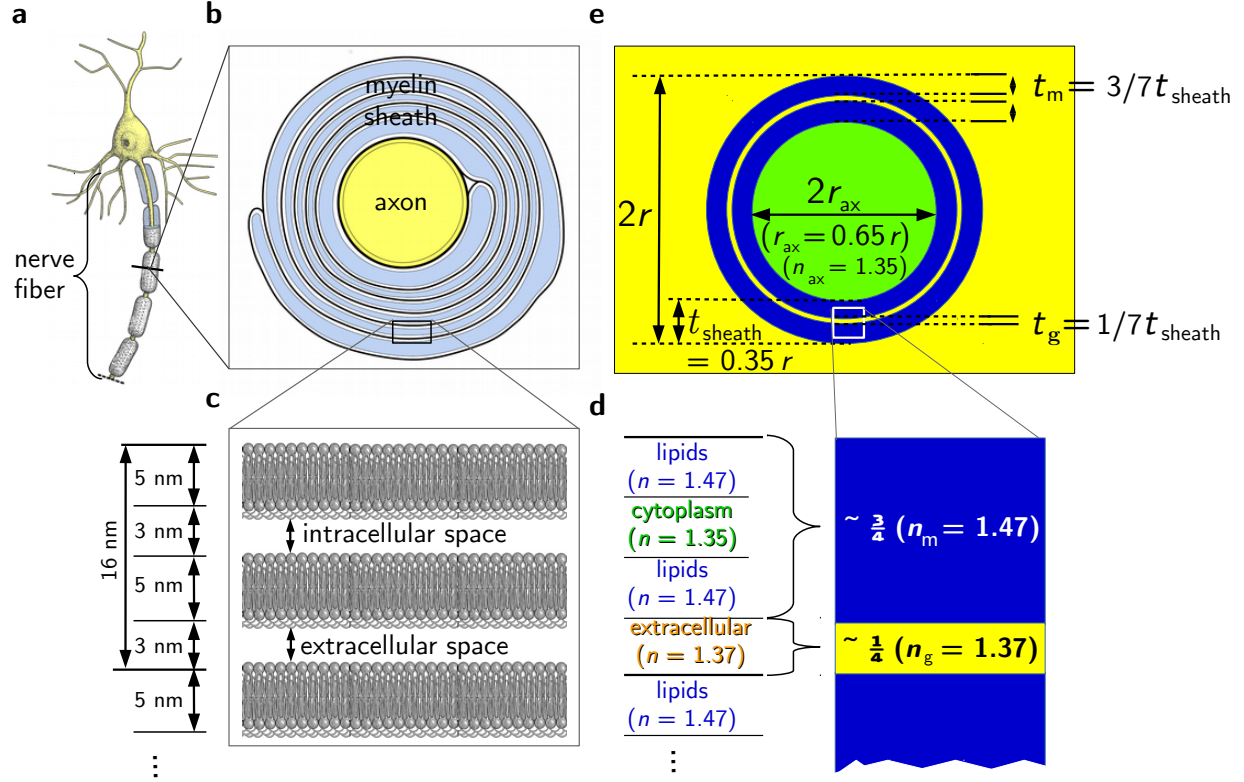


**Fig. 15. Supplementary Figure | Modeling nerve fibers.** **a** Schematic drawing of a nerve fiber. **b** Cross-section through the nerve fiber showing the inner axon and the surrounding myelin sheath (formed by oligodendrocytes which are spirally wrapped around the axon). **c** Schematic representation of the myelin structure consisting of several lipid bilayers (5 nm thick cell membranes) with an intracellular/cytoplasmic and extracellular space of about 3 nm. **d** Each cell layer (two lipid bilayers with separating cytoplasm) was considered as one “myelin layer” with an effective refractive index  $n_m = 1.47$  (blue), the extracellular space was considered to be filled with glycerin solution (“glycerin layer”) with a refractive index  $n_g = 1.37$  (yellow). The myelin and glycerin layers were assumed to contribute  $3/4$  and  $1/4$  to the overall myelin sheath thickness  $t_{sheath}$ , respectively. **e** Nerve fibers were modeled with double myelin layers with thickness  $t_m = 3/7 t_{sheath}$  and a single separating glycerin layer with thickness  $t_g = 1/7 t_{sheath}$ . The myelin sheath thickness contributes approximately one third to the overall fiber radius ( $t_{sheath} = 0.35r$ ). The inner axon was modeled with a radius  $r_{ax} = 0.65r$  and a refractive index  $n_{ax} = 1.35$ .

### Supplementary Note 3. Computation of the transmitted light intensities

The computation of the transmitted light intensities consists of several steps:

**1.) Maxwell Solver:** After passing the polarizing filters in front of the sample (see Fig. 10 on the left), the light wave is left-handed circularly polarized. The propagation of the light wave through the sample was computed by TDME3D (see Methods). The resulting light wave is represented by a superposition of monochromatic plane waves with different wave vectors  $\vec{k}$  and real amplitudes  $\vec{E}_{0,k}$ :

$$\vec{E}_k(\vec{r}, t) = \vec{E}_{0,k} \cos(\vec{k} \cdot \vec{r} - \omega t + \phi) \quad (1)$$

$$\equiv \vec{A}_k \cos(\vec{k} \cdot \vec{r} - \omega t) - \vec{B}_k \sin(\vec{k} \cdot \vec{r} - \omega t), \quad (2)$$

where  $\vec{r}$  and  $t$  are the spatial and temporal coordinates,  $\omega$  is the angular frequency,  $\phi$  is the phase, and  $\vec{A}_k$  and  $\vec{B}_k$  are defined as:  $\vec{A}_k = \vec{E}_{0,k} \cos \phi$  and  $\vec{B}_k = \vec{E}_{0,k} \sin \phi$ .

Note that every index  $k$  denotes a different wave vector  $\vec{k}$  and is not related to the wave number  $k = 2\pi/\lambda$  (the wavelength of the transmitted light waves is the same as for the ingoing light wave).

**2.) Yee Shift:** Before further processing, the electromagnetic field components were shifted in the x,y,z-direction to the middle of the corresponding Yee cell, respectively:

$$E_{k,x}(\vec{r}, t) : y \mapsto y + \Delta y/2, \quad z \mapsto z + \Delta z/2, \quad (3)$$

$$E_{k,y}(\vec{r}, t) : x \mapsto x + \Delta x/2, \quad z \mapsto z + \Delta z/2, \quad (4)$$

$$E_{k,z}(\vec{r}, t) : x \mapsto x + \Delta x/2, \quad y \mapsto y + \Delta y/2, \quad (5)$$

where  $\Delta x = \Delta y = \Delta z$  is the side length of the cubic Yee cell.

For each shift  $\Delta j$  in the direction  $j = \{x, y, z\}$ , the vector components  $A_{k,i}$  and  $B_{k,i}$  were recomputed as follows:

$$\check{A}_{k,i} = A_{k,i} \cos(k_j \Delta j) - B_{k,i} \sin(k_j \Delta j), \quad (6)$$

$$\check{B}_{k,i} = A_{k,i} \sin(k_j \Delta j) + B_{k,i} \cos(k_j \Delta j). \quad (7)$$

After performing the shifts specified in Eqs. (3) and (5), the resulting field vector is given by:

$$\vec{E}'_k(\vec{r}, t) = \vec{A}'_k \cos(\vec{k} \cdot \vec{r} - \omega t) - \vec{B}'_k \sin(\vec{k} \cdot \vec{r} - \omega t). \quad (8)$$

**3.) Scattering Pattern:** To study how much light is scattered under a certain angle (wave vector  $\vec{k}$ ), the *scattering pattern* was computed, i. e. the intensity per wave vector normalized by the ingoing light intensity ( $I_0$ ) per image pixel (px):

$$I_k \equiv \frac{|\vec{E}'_{0,k}|^2}{I_0/(\# \text{px})} = \frac{|\vec{A}'_k|^2 + |\vec{B}'_k|^2}{I_0/(\# \text{px})}. \quad (9)$$

**4.) Rotating Analyzer:** To model the 3D-PLI measurement, the electric field vector  $\vec{E}'_k(\vec{r}, t)$  was processed through a second linear polarizer (*analyzer*) rotated by angles  $\rho$ , yielding:

$$\vec{\check{E}}_k(\vec{r}, t, \rho) = \vec{A}'_k(\rho) \cos(\vec{k} \cdot \vec{r} - \omega t) - \vec{B}'_k(\rho) \sin(\vec{k} \cdot \vec{r} - \omega t). \quad (10)$$

The x- and y-components of  $\vec{\check{E}}_k(\vec{r}, t, \rho)$  were computed by multiplying  $\vec{E}'_k(\vec{r}, t)$  with the Jones matrix of a rotated linear polarizer [45]:

$$\begin{aligned} \begin{pmatrix} \check{E}_{k,x}(\vec{r}, t, \rho) \\ \check{E}_{k,y}(\vec{r}, t, \rho) \end{pmatrix} &= \begin{pmatrix} \cos \rho & -\sin \rho \\ \sin \rho & \cos \rho \end{pmatrix} \begin{pmatrix} 0 & 0 \\ 0 & 1 \end{pmatrix} \begin{pmatrix} \cos \rho & \sin \rho \\ -\sin \rho & \cos \rho \end{pmatrix} \begin{pmatrix} E'_{k,x}(\vec{r}, t) \\ E'_{k,y}(\vec{r}, t) \end{pmatrix} \\ &= \begin{pmatrix} \sin \rho (E'_{k,x}(\vec{r}, t) \sin \rho - E'_{k,y}(\vec{r}, t) \cos \rho) \\ -\cos \rho (E'_{k,x}(\vec{r}, t) \sin \rho - E'_{k,y}(\vec{r}, t) \cos \rho) \end{pmatrix}. \end{aligned} \quad (11)$$

The z-component was computed by applying Maxwell's equation in free space and assuming  $\vec{\check{E}}_k(\vec{r}, t, \rho) = \vec{E}_{0,k}(\rho) e^{i(\vec{k} \cdot \vec{r} - \omega t + \phi)}$  (plane monochromatic wave):

$$\text{div} \vec{\check{E}}_k(\vec{r}, t, \rho) = 0 \quad \Leftrightarrow \quad \vec{k} \cdot \vec{\check{E}}_k(\vec{r}, t, \rho) = 0 \quad (12)$$

$$\begin{aligned} \Leftrightarrow \check{E}_{k,z}(\vec{r}, t, \rho) &= -\frac{1}{k_z} (k_x \check{E}_{k,x}(\vec{r}, t, \rho) + k_y \check{E}_{k,y}(\vec{r}, t, \rho)) \\ &\stackrel{(11)}{=} -\frac{k_x \sin \rho - k_y \cos \rho}{k_z} (E'_{k,x}(\vec{r}, t) \sin \rho - E'_{k,y}(\vec{r}, t) \cos \rho). \end{aligned} \quad (13)$$

**5.) Objective Lens:** The objective lens was assumed to be ideal and both specimen and detector were assumed to lie within the corresponding focal planes of the lens. Thus, the propagation of the electromagnetic wave between sample and detector was assumed to be free and  $\vec{\check{E}}_k(\vec{r}, t, \rho)$  was evaluated at the z-position of the detection plane behind the

sample (defined as  $z = 0$ ):

$$\vec{r} = (r_x, r_y, 0)^T. \quad (14)$$

To account for the numerical aperture (NA) of the objective lens, only  $k$ -vectors were processed that fulfill:

$$\theta_k = \arccos\left(\frac{k_z}{\sqrt{k_x^2 + k_y^2 + k_z^2}}\right) \leq \arcsin(\text{NA}). \quad (15)$$

**6.) Detector Microlenses:** The detector microlenses of the camera were modeled by applying a moving average over the area of the microlens with radius  $r_0 = 0.665 \mu\text{m}$ :

$$\vec{E}_k(\vec{r}, t, \rho) = \vec{E}_k(\vec{r}, t, \rho) * \text{circ}(r), \quad \text{circ}(r) = \begin{cases} \frac{1}{\pi r_0^2}, & r < r_0 \\ 0, & r \geq r_0. \end{cases} \quad (16)$$

**7.) Intensity:** In principle, the intensity detected by the camera sensor depends on the angle of incidence of the incident light:  $I \cos \theta_k$ . As the numerical aperture is sufficiently small ( $\text{NA} = \sin \theta_k \approx 0.15 \Leftrightarrow \cos \theta_k > 0.9886$ ), the angle dependence was neglected, which enables to represent the intensity  $I(\vec{r}, \rho)$  as Fourier series in  $\rho$ , as described below.

With this assumption, the light intensity recorded by the camera is given by the absolute squared value of the electric field vector. To compute the intensity at a certain point  $\vec{r}$  in the image plane, the electric field vectors were summed over  $\vec{k}$  and averaged over time:

$$\begin{aligned} I(\vec{r}, \rho) &\propto |\vec{E}(\vec{r}, \rho)|^2 \equiv \frac{1}{T} \int_0^T \left| \sum_{\vec{k}} \vec{E}_k(\vec{r}, t, \rho) \right|^2 dt \\ &\propto \left| \text{FT}^{-1} \left\{ \vec{A}_k(\rho) + i \vec{B}_k(\rho) \right\} * \text{circ}(r) \right|^2, \end{aligned} \quad (17)$$

where  $\text{FT}^{-1}$  denotes the *inverse discrete Fourier transform*:

$$\text{FT}^{-1}\{f\} = \sum_{\vec{k}} f_{\vec{k}} e^{i\vec{k}\cdot\vec{r}}. \quad (18)$$

The *discrete Fourier transform (FT)* is defined analogously.

To save computing time, the convolution in Eq. (17) was replaced by a multiplication, making use of the *convolution theorem*:

$$I(\vec{r}, \rho) \propto \left| \text{FT}^{-1} \left\{ \left( \vec{A}_k(\rho) + i \vec{B}_k(\rho) \right) \cdot \text{FT}\{\text{circ}(r)\} \right\} \right|^2 \quad (19)$$

$$= \left| \text{FT}^{-1} \left\{ \left( \vec{A}_k(\rho) + i \vec{B}_k(\rho) \right) \cdot 2 \frac{J_1(r_0 k_{xy})}{r_0 k_{xy}} \right\} \right|^2, \quad (20)$$

where the function  $J_1(x)$  is the Bessel function of the first kind of order one, with  $k_{xy} \equiv \sqrt{k_x^2 + k_y^2}$  and  $r_0 = 0.665 \mu\text{m}$ .

To simplify notation, the following abbreviations are defined:

$$\vec{\mathcal{E}}_k(\rho) \equiv \left( \vec{A}_k(\rho) + i \vec{B}_k(\rho) \right) \cdot 2 \frac{J_1(r_0 k_{xy})}{r_0 k_{xy}}, \quad \vec{\mathcal{E}}(\vec{r}, \rho) \equiv \text{FT}^{-1} \left\{ \vec{\mathcal{E}}_k(\rho) \right\}, \quad (21)$$

$$\vec{\mathcal{E}}'_k \equiv \left( \vec{A}'_k + i \vec{B}'_k \right) \cdot 2 \frac{J_1(r_0 k_{xy})}{r_0 k_{xy}}, \quad \vec{\mathcal{E}}'(\vec{r}) \equiv \text{FT}^{-1} \left\{ \vec{\mathcal{E}}'_k \right\}. \quad (22)$$

The intensity is then given by:

$$I(\vec{r}, \rho) \propto |\vec{\mathcal{E}}_x(\vec{r}, \rho)|^2 + |\vec{\mathcal{E}}_y(\vec{r}, \rho)|^2 + |\vec{\mathcal{E}}_z(\vec{r}, \rho)|^2. \quad (23)$$

The x- and y-components of the electric field vector  $\vec{E}'_k(\vec{r}, t, \rho)$  behind the rotating analyzer were computed from  $\vec{E}'_k(\vec{r}, t) = \vec{A}'_k \cos(\vec{k} \cdot \vec{r} - \omega t) - \vec{B}'_k \sin(\vec{k} \cdot \vec{r} - \omega t)$  according to Eq. (11). As the equation is linear in the x- and y-components of  $\vec{E}'_k(\vec{r}, t)$ , the x- and y-components of  $\{\vec{A}'_k, \vec{B}'_k, \vec{E}'_k\}$  are transformed to  $\{\vec{A}_k(\rho), \vec{B}_k(\rho), \vec{E}_k(\rho)\}$  according to the same equation. As the Fourier transform is independent from  $\rho$ , Eq. (11) also holds for the x- and y-components of  $\vec{\mathcal{E}}'(\vec{r})$  and  $\vec{\mathcal{E}}(\vec{r}, \rho)$ , yielding Fourier coefficients of order zero and two:

$$\begin{aligned} & |\vec{\mathcal{E}}_x(\vec{r}, \rho)|^2 + |\vec{\mathcal{E}}_y(\vec{r}, \rho)|^2 \\ & \stackrel{(11)}{=} \sin^2 \rho |\mathcal{E}'_x(\vec{r})|^2 + \cos^2 \rho |\mathcal{E}'_y(\vec{r})|^2 - \sin \rho \cos \rho \left( \mathcal{E}'_x(\vec{r}) \mathcal{E}'_y{}^*(\vec{r}) + \mathcal{E}'_x{}^*(\vec{r}) \mathcal{E}'_y(\vec{r}) \right) \\ & = \frac{1}{2} \underbrace{\left( |\mathcal{E}'_x(\vec{r})|^2 + |\mathcal{E}'_y(\vec{r})|^2 \right)}_{c_0} + \frac{1}{2} \underbrace{\left( |\mathcal{E}'_y(\vec{r})|^2 - |\mathcal{E}'_x(\vec{r})|^2 \right)}_{c_2} \cos(2\rho) \\ & \quad - \frac{1}{2} \underbrace{\left( \mathcal{E}'_x(\vec{r}) \mathcal{E}'_y{}^*(\vec{r}) + \mathcal{E}'_x{}^*(\vec{r}) \mathcal{E}'_y(\vec{r}) \right)}_{d_2} \sin(2\rho) \end{aligned} \quad (24)$$

$$\equiv c_0(\vec{r}) + c_2(\vec{r}) \cos(2\rho) + d_2(\vec{r}) \sin(2\rho), \quad (25)$$

where the trigonometric identities  $(\cos^2 x = \frac{1}{2} + \frac{1}{2} \cos(2x), \sin x \cos x = \frac{1}{2} \sin(2x))$  have been used.

Similar analytical calculations yield Fourier coefficients of orders zero, two, and four:

$$\begin{aligned} |\vec{\mathcal{E}}_z(\vec{r}, \rho)|^2 &= e_0(\vec{r}) + e_2(\vec{r}) \cos(2\rho) + f_2(\vec{r}) \sin(2\rho) \\ & \quad + e_4(\vec{r}) \cos(4\rho) + f_4(\vec{r}) \sin(4\rho), \end{aligned} \quad (26)$$

where  $e_m(\vec{r})$  and  $f_m(\vec{r})$  are functions of the inverse discrete Fourier transforms:

$$X_x(\vec{r}) \equiv \text{FT}^{-1} \left\{ \frac{k_x}{k_z} \mathcal{E}'_{k,x} \right\}, \quad X_y(\vec{r}) \equiv \text{FT}^{-1} \left\{ \frac{k_y}{k_z} \mathcal{E}'_{k,x} \right\}, \quad (27)$$

$$Y_x(\vec{r}) \equiv \text{FT}^{-1} \left\{ \frac{k_x}{k_z} \mathcal{E}'_{k,y} \right\}, \quad Y_y(\vec{r}) \equiv \text{FT}^{-1} \left\{ \frac{k_y}{k_z} \mathcal{E}'_{k,y} \right\}. \quad (28)$$

Thus, the transmitted light intensity  $I(\vec{r}, \rho)$  can be written in terms of a Fourier series:

$$\begin{aligned} I(\vec{r}, \rho) &\propto |\vec{\mathcal{E}}_x(\vec{r}, \rho)|^2 + |\vec{\mathcal{E}}_y(\vec{r}, \rho)|^2 + |\vec{\mathcal{E}}_z(\vec{r}, \rho)|^2 \\ &= a_0(\vec{r}) + a_2(\vec{r}) \cos(2\rho) + b_2(\vec{r}) \sin(2\rho) \\ & \quad + a_4(\vec{r}) \cos(4\rho) + b_4(\vec{r}) \sin(4\rho), \end{aligned} \quad (29)$$

$$\begin{aligned} a_0(\vec{r}) &\equiv c_0(\vec{r}) + e_0(\vec{r}), \quad a_2(\vec{r}) \equiv c_2(\vec{r}) + e_2(\vec{r}), \\ b_2(\vec{r}) &\equiv d_2(\vec{r}) + f_2(\vec{r}), \quad a_4(\vec{r}) \equiv e_4(\vec{r}), \quad b_4(\vec{r}) \equiv f_4(\vec{r}), \end{aligned} \quad (30)$$

where the Fourier coefficients  $a_m(\vec{r})$  and  $b_m(\vec{r})$  are computed from the six inverse discrete Fourier transforms defined above:  $\mathcal{E}'_x(\vec{r}), \mathcal{E}'_y(\vec{r}), X_x(\vec{r}), X_y(\vec{r}), Y_x(\vec{r}), Y_y(\vec{r})$ .

For non-normally incident light ( $k_x \neq 0$  or  $k_y \neq 0$ ), the transmitted light intensity contains Fourier coefficients of order four (cf. Eqs. (26) to (28)).

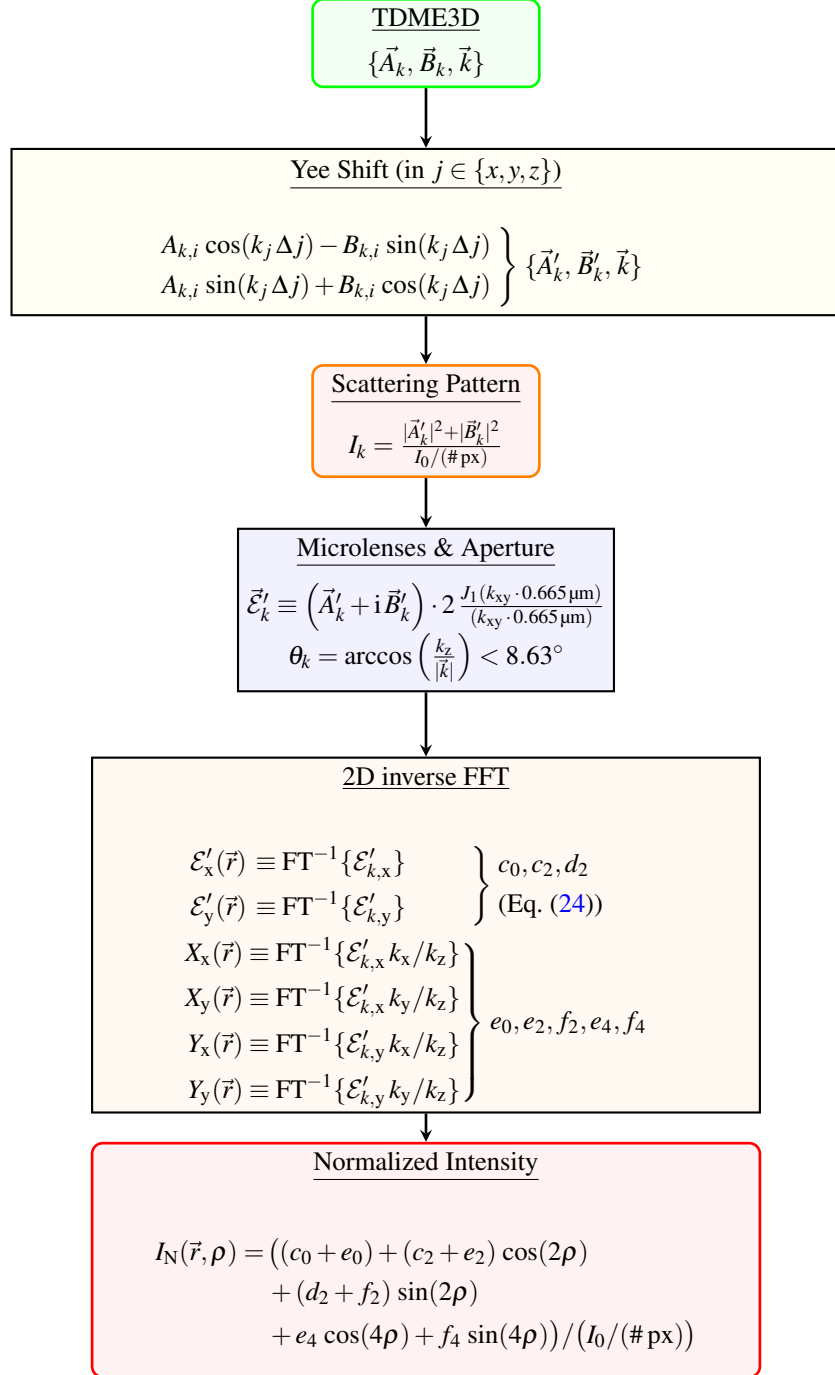


**Fig. 16. Supplementary Figure | Flow chart visualizing the computation of the transmitted light intensities.** The electromagnetic field components behind the sample (represented by a set of vectors  $\{\vec{A}_k, \vec{B}_k, \vec{k}\}$ , green box) were computed by the Maxwell Solver (TDME3D). The field components were shifted to the middle of the corresponding Yee cell (with side length  $\Delta$ ). To study how much light is scattered under a certain angle (wave vector  $\vec{k}$ ), the scattering pattern  $I_k$  was computed, i.e. the intensity per wave vector normalized by the ingoing light intensity  $I_0$  per image pixel (orange box). The spherical microlenses of the camera detector were modeled by applying a moving average over the area of the microlens with radius  $0.665 \mu\text{m}$  ( $J_1$  is the Bessel function of the first kind of order one). The numerical aperture of the imaging system was modeled by considering only waves with directions of propagation  $\vec{k}$  that fulfill  $\theta_k < \arcsin(\text{NA}) \approx 8.63^\circ$ . Applying a 2D inverse discrete Fast Fourier Transform (FFT), the transmitted light intensities were computed and normalized by the ingoing light intensity per pixel (red box).

Using Eq. (29), the light intensity was computed for arbitrary rotation angles  $\rho$  and normalized by the ingoing light intensity per pixel:

$$I_N(\vec{r}, \rho) = \frac{I(\vec{r}, \rho)}{I_0 / (\# \text{px})}. \quad (31)$$

In the experiment, the measured light intensities are normalized by the light intensities measured without specimen to compensate for filter inhomogeneities. This image calibration could be modeled by performing an additional simulation run without sample. To save computing time, the simulated light intensities were simply normalized by  $I_0$  (without considering the imaging system) and only relative values were used for the comparison between measured and simulated light intensities.

The Fourier coefficient of order zero  $a_{0,N}(\vec{r})$  obtained from the simulated normalized transmitted light intensity  $I_N(\vec{r}, \rho)$  via Eqs. (30) and (31) was used to compute the simulated transmittance images  $I_{T,N}(\vec{r})$ :

$$I_{T,N}(\vec{r}) \equiv a_{0,N}(\vec{r}). \quad (32)$$

**Implementation:** Supplementary Fig. 16 summarizes the most important steps of computing the transmitted light intensities for 3D-PLI simulations. The computation was carried out in *Python* (version 2.7.6) using the *NumPy* package (version 1.12.1) [46, 47]. To obtain the intensity at a certain pixel position  $(x, y)$ , the inverse discrete Fourier transform was computed in two dimensions by means of the *Fast Fourier Transform* [48]. To enable an efficient use of the FFT, the number of grid points in  $x$  and  $y$  ( $N_x$  and  $N_y$ ) were set to be a multiple of 2:

$$N'_x = 2^{m_x} > N_x, \quad (33)$$

$$N'_y = 2^{m_y} > N_y. \quad (34)$$

#### Supplementary Note 4. Evaluation of simulation parameters

The transmittance images were simulated for different simulation parameters: different numbers of myelin layers  $L$ , different Yee mesh sizes  $\Delta$ , different wavelengths  $\lambda$ , and different angles of incidence  $\theta$ . To estimate the impact of the simulation parameters on the simulation results, only one simulation parameter was varied while all other simulation parameters were chosen as in Supplementary Tab. 2. If not otherwise stated, the simulations were performed for normally incident light with a wavelength of 550 nm.

To estimate the accuracy of the resulting transmittance images, the *absolute relative difference between the mean values (ARDM)* and the *relative mean absolute difference (RMAD)* between the images were computed:

$$\text{ARDM} \equiv \left| \frac{\langle \text{image} \rangle - \langle \text{ref.image} \rangle}{\langle \text{ref.image} \rangle} \right|, \quad (35)$$

$$\text{RMAD} \equiv \frac{\langle |\text{image} - \text{ref.image}| \rangle}{|\langle \text{ref.image} \rangle|}. \quad (36)$$

In this notation, the “image” refers to the transmittance image for which the absolute relative difference is computed (obtained e. g. from simulations with different Yee mesh sizes). The “reference image” is the transmittance image used for comparison (obtained e. g. from the simulation with minimum mesh size). The symbol  $\langle \rangle$  represents the average over all image pixels.

#### *Different numbers of myelin layers*

The simulations in the main part were performed with double myelin layers (cf. Supplementary Fig. 15e) and a Yee mesh size  $\Delta = 25$  nm. To estimate the impact of the reduced number of myelin layers on the simulation results, a straight single fiber with reduced simulation volume (see Supplementary Fig. 17a) was simulated for different numbers  $L$  of myelin layers with thickness  $t_m$  (and  $L - 1$  separating glycerin layers with thickness  $t_g = t_m/3$ ) as well as for a realistic model of the myelin sheath consisting of 43 thin layers (see Supplementary Fig. 17b). The Yee mesh size was chosen to be small enough to resolve all geometric features: For most samples, the mesh size was chosen to be one third of the glycerin layer thickness ( $\Delta = t_g/3$ ). Fibers with two myelin layers ( $L = 2$ ) were also simulated for larger mesh sizes ( $\Delta = t_g/2 = 12.5$  nm and  $\Delta = t_g = 25$  nm). The realistic myelin sheath was simulated for  $\Delta = t_g = 3$  nm.

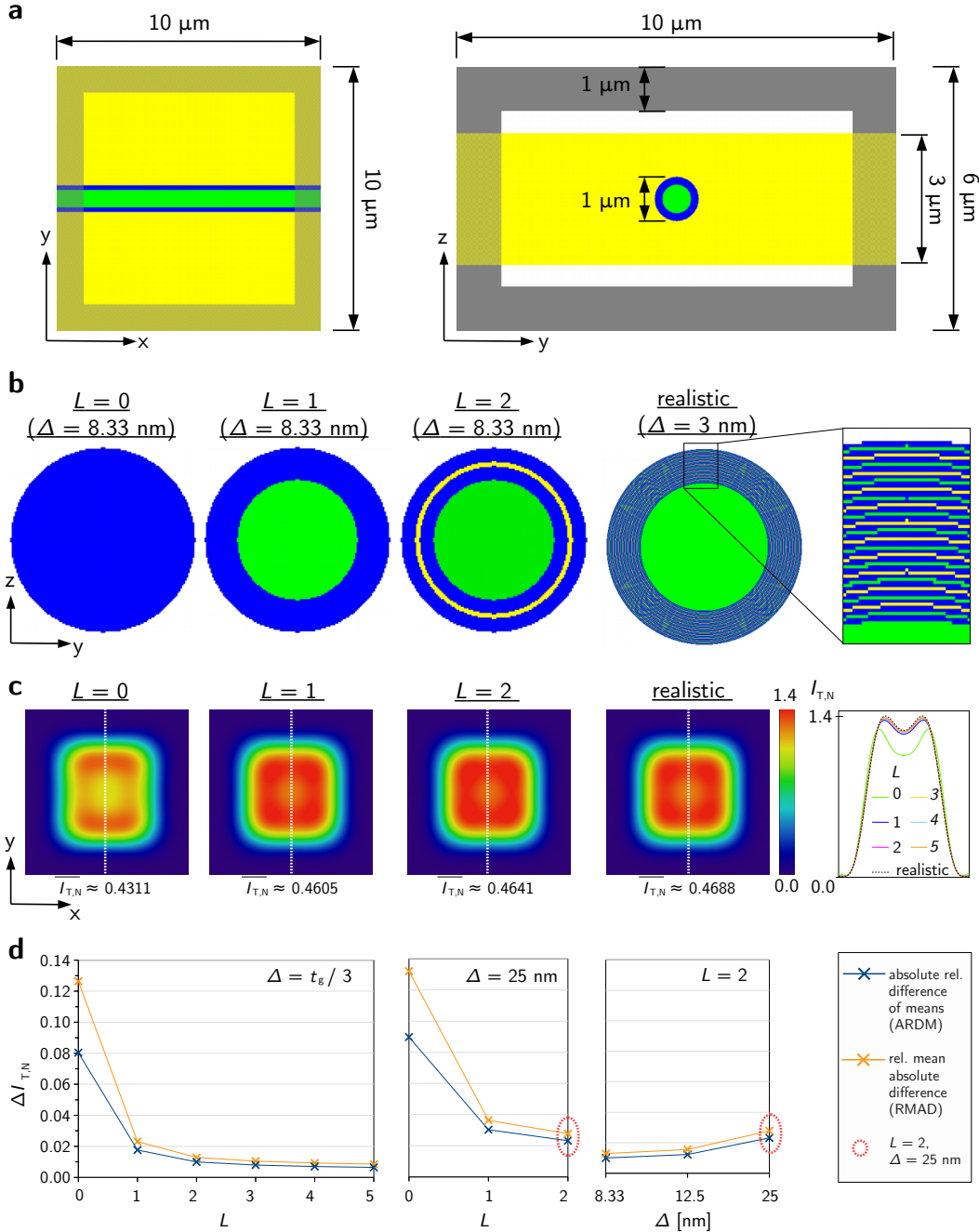


**Fig. 17. Supplementary Figure | Error estimation for different numbers of myelin layers.** **a** Dimensions of the simulation volume used to simulate a straight single fiber with different numbers of myelin layers. **b** Cross-section through fibers with different numbers  $L$  of myelin layers and different Yee mesh sizes  $\Delta$ . All fibers were modeled with a diameter of  $1 \mu\text{m}$ , consisting of an inner axon (green) with a diameter of  $0.65 \mu\text{m}$  and a surrounding myelin sheath with a thickness of  $0.175 \mu\text{m}$ . The myelin sheath is composed of alternating layers of myelin (blue) and glycerin (yellow), the myelin layers are three times thicker than the glycerin layers. The realistic model of the myelin sheath contains 22 layers of  $5 \text{ nm}$  thick cell membranes (blue), interrupted by  $3 \text{ nm}$  thick alternating layers of cytoplasm (green) and surrounding glycerin solution (yellow), yielding a myelin sheath composed of 43 thin layers. The refractive indices are 1.35 for the axon/cytoplasm (green), 1.37 for the glycerin solution (yellow), and 1.47 for the myelin layers (blue). A motivation of the myelin sheath model and the corresponding refractive indices can be found in Supplementary Fig. 15. **c** Normalized transmittance images, corresponding mean values  $\bar{I}_{T,N}$ , and transmittance profiles (middle image pixels evaluated along the  $y$ -axis, see white dashed lines) obtained from 3D-PLI simulations with different numbers  $L$  of myelin layers and Yee mesh sizes defined in (b). The simulations were performed as described in Methods (using a normally incident plane wave with  $550 \text{ nm}$  wavelength and simulations parameters specified in Supplementary Tab. 2). The profiles with non-italic labels belong to the displayed transmittance images. **d** Relative differences between the transmittance images with different numbers  $L$  of myelin layers and different mesh sizes  $\Delta$  (relative to the glycerin layer thickness  $t_g$ ) and the transmittance image with realistic myelin sheath. The values for ARDM (blue) and RMAD (orange) were computed using Eq. (35) and Eq. (36), the values surrounded in red belong to fibers with double myelin layers ( $L = 2$ ) and  $25 \text{ nm}$  mesh size, which were used for the simulations in the main part.

Supplementary Fig. 17c shows the corresponding transmittance images, mean values, and line profiles obtained from 3D-PLI simulations with normally incident light and  $\lambda = 550$  nm for the straight single fibers shown in Supplementary Fig. 17b. The mean values and line profiles for  $L \geq 1$  look similar. For better comparison, Supplementary Fig. 17d shows the absolute relative differences (ARDM and RMAD) between the transmittance images with  $L = \{0, 1, 2, 3, 4, 5\}$  and the transmittance image with realistic myelin sheath. The relative differences decrease with increasing number of myelin layers  $L$  and with decreasing mesh size  $\Delta$ . A fiber with two or more myelin layers and a mesh size  $\Delta = t_g/3$  yields similar transmittance values as the fiber with realistic myelin sheath. With increasing mesh size, the relative differences increase. For a fiber with double myelin layers and a mesh size  $\Delta = 12.5$  nm (25 nm), the differences are: ARDM  $\approx 1.2\%$  (2.3%) and RMAD  $\approx 1.6\%$  (2.8%). For a mesh size of 25 nm, the differences are still smaller than for a fiber without or with a single myelin layer. Thus, a fiber with double myelin layers and a mesh size of 25 nm is a good compromise between accuracy and computing time. In interesting cases, the simulations were repeated for a reduced mesh size ( $\Delta = 12.5$  nm), see black crosses in Supplementary Fig. 18b.

#### Different wavelengths, angles of incidence, and Yee mesh sizes

According to manufacturer information, the light source of the employed polarizing microscope emits light with slightly different wavelengths ( $\lambda = (550 \pm 5)$  nm) and different angles of incidence (the sample is illuminated under angles  $\vartheta < 3^\circ$ ). The simulations in the main part were only performed for normally incident light and a single wavelength ( $\lambda = 550$  nm). To estimate the accuracy of the simulation results, especially for the transmittance curves in Fig. 3c, the 3D-PLI simulations for the bundle of densely grown fibers were performed for different wavelengths ( $\lambda = \{545, 550, 555\}$  nm) and different angles of incidence ( $\theta = 0^\circ$ ;  $\theta = 3^\circ$ ,  $\varphi = \{0^\circ, 90^\circ, 180^\circ, 270^\circ\}$ ) for inclination angles  $\alpha = \{0, 10, \dots, 90\}^\circ$ . The resulting transmittance curves for NA = 0.15 (solid curves) and NA = 1 (dashed curves) are shown in Supplementary Fig. 18b. The simulations were performed for a Yee mesh size of 25 nm. For some inclination angles, the simulations for NA = 0.15 were repeated for a smaller mesh size ( $\Delta = 12.5$  nm), see black crosses.

The transmittance curves for different wavelengths and for diffusive light (obtained from simulation runs with different angles of incidence) look all very similar. The maximum difference between the normalized transmittance values is less than 0.03. In addition, the simulations with smaller mesh size (black crosses) yield similar results as the simulations with larger mesh size (curves), the maximum difference between the normalized transmittance values is only about 0.005. Thus, the transmittance curves for the bundle of densely grown fibers are not sensitive to small changes in wavelength, angle of incidence, or mesh size, which demonstrates the validity of the simulation results.

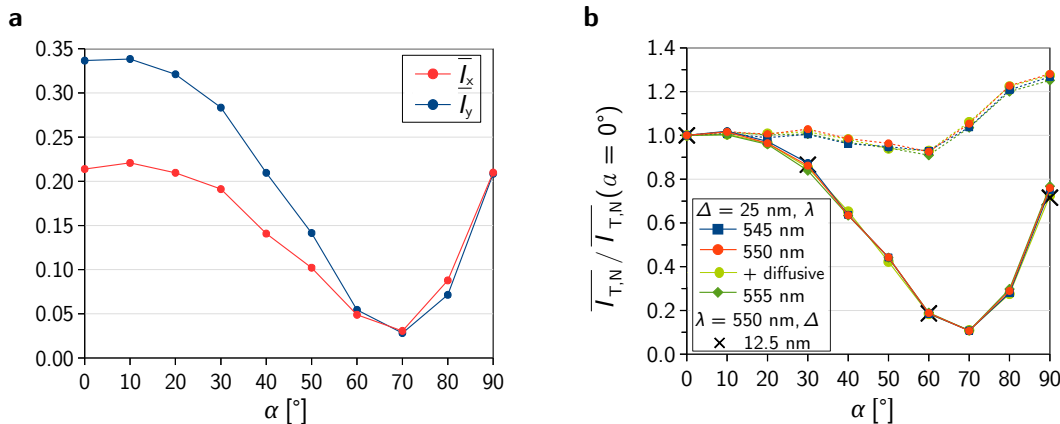


**Fig. 18. Supplementary Figure | Simulated transmitted light intensity for different simulation parameters.** Bundle of densely grown fibers (cf. Fig. 3a) simulated for different inclination angles  $\alpha$ : **a** Mean transmitted light intensity for light polarized along the x-axis ( $\bar{I}_x$ ) or along the y-axis ( $\bar{I}_y$ ) plotted against  $\alpha$ . The simulations were performed as described in Methods for a numerical aperture NA = 0.15 (using a normally incident plane wave with 550 nm wavelength and simulation parameters specified in Supplementary Tab. 2). **b** Transmittance curves (mean transmittance value  $\bar{I}_{T,N}$  plotted against  $\alpha$ ) obtained from 3D-PLI simulations (see Methods) for normally incident light with different wavelengths  $\lambda = \{545, 550, 555\}$  nm and different Yee mesh sizes  $\Delta = \{25, 12.5\}$  nm. The simulations for  $\lambda = 550$  nm and  $\Delta = 25$  nm were also performed for diffusive light (with angles of incidence  $\{\theta = 0^\circ\}$ ,  $\{\theta = 3^\circ; \varphi = 4 \times 90^\circ\}$ ). The curves were normalized by the mean transmittance value of the horizontal bundle, respectively. The solid curves were computed for the numerical aperture of the imaging system (NA = 0.15), the dashed curves were computed for NA = 1.

Structure	Rat		Vervet	
	Coronal	Sagittal	Coronal	Sagittal
ac	–	–	–	$0.11 \pm 0.04$
cc	$0.33 \pm 0.16$	$0.09 \pm 0.04$	$0.24 \pm 0.09$	$0.11 \pm 0.05$
cg	$0.15 \pm 0.06$	$0.18 \pm 0.09$	$0.08 \pm 0.02$	$0.24 \pm 0.09$
df	$0.10 \pm 0.03$	–	–	–
f	–	–	$0.13 \pm 0.06$	$0.26 \pm 0.10$
fi	$0.25 \pm 0.10$	$0.15 \pm 0.07$	–	–
sm	$0.08 \pm 0.03$	–	–	–

Table 1: **Supplementary Table | Transmittance values in regions with flat and steep fibers.** The table shows the mean transmittance values ( $\overline{T_{T,N}}$ ) and the standard deviation for the selected white matter regions in Fig. 1. For better comparison, the values are surrounded by frames in the same color. Regions with flat (in-plane) fiber structures in green show larger transmittance values than regions with steep (out-of-plane) fiber structures in yellow. The fiber structure in the cingulum (cg) might be inhomogeneous so that a distinction between flat and steep fibers is not straightforward. Therefore, the corresponding transmittance values are highlighted in italics.

<u>General Simulation Parameters</u>	
• Yee mesh size:	$\Delta = 25 \text{ nm}$
• Courant factor:	$C = 0.8$
• # time steps:	200
• MPI grid:	$16 \times 16 \times 16$
• CPU hours:	$\sim 7000\text{--}8000$
• wall time:	$\sim 1:45\text{--}2:00 \text{ h}$
• min. memory required:	$\sim 260\text{--}360 \text{ GB}$
<u>Simulation Box</u>	
• volume:	$x \times y \times z = 30 \times 30 \times 35 \text{ } \mu\text{m}^3$
• boundaries:	UPML ( $1 \text{ } \mu\text{m}$ thick)
<u>Surrounding Medium</u>	
• dimensions:	$x \times y \times z = 30 \times 30 \times 31 \text{ } \mu\text{m}^3$
• refractive index:	$n_{\text{surr}} = 1.37$
<u>Fiber Configuration</u>	
• volume:	$x \times y \times z = 30 \times 30 \times 30 \text{ } \mu\text{m}^3$
• fiber radius:	$r \sim 0.5 \text{ } \mu\text{m}$
• axon:	$r_{\text{ax}} = 0.65r, \quad n_{\text{ax}} = 1.35$
• myelin sheath:	$t_{\text{sheath}} = 0.35r = t_{\text{m}} + t_{\text{g}} + t_{\text{m}}$
• double myelin layers:	$t_{\text{m}} = \frac{3}{7}t_{\text{sheath}}, \quad n_{\text{m}} = 1.47$
• single glycerin layer:	$t_{\text{g}} = \frac{1}{7}t_{\text{sheath}}, \quad n_{\text{g}} = 1.37$

Table 2: **Supplementary Table | Simulation parameters.** The table shows the simulation parameters used for simulating the fiber configurations in the main part. The fibers were modeled with radius  $r$  and double myelin layers with thicknesses  $t$  and refractive indices  $n$  (see Supplementary Fig. 15d,e). The fiber configurations were generated in a volume of  $30 \times 30 \times 30 \text{ } \mu\text{m}^3$ , surrounded by a medium with dimensions  $30 \times 30 \times 31 \text{ } \mu\text{m}^3$  and a refractive index of 1.37 (glycerin solution). The sample was placed in a simulation box of  $30 \times 30 \times 35 \text{ } \mu\text{m}^3$ , surrounded by  $1 \text{ } \mu\text{m}$  thick uniaxial perfectly matched layer (UPML) boundaries (cf. Supplementary Fig. 11a in gray). Apart from dimensions and refractive indices, the table also lists more general simulation parameters and the expenses of one simulation run on JUQUEEN [32] (computation of one fiber configuration, one wavelength, and one angle of incidence).